



Defence Research and
Development Canada

Recherche et développement
pour la défense Canada



RANS calculations of the evolution of vortices on unstructured grids

David Hally

Defence R&D Canada – Atlantic

Technical Memorandum
DRDC Atlantic TM 2009-052
November 2009

Canada

This page intentionally left blank.

RANS calculations of the evolution of vortices on unstructured grids

David Hally

Defence R&D Canada – Atlantic

Technical Memorandum

DRDC Atlantic TM 2009-052

November 2009

Principal Author

Original signed by David Hally

David Hally

Approved by

Original signed by D. Hopkin

D. Hopkin
Head/Maritime Asset Protection

Approved for release by

Original signed by Ron Kuwahara for

C. Hyatt
Head/Document Review Panel

ANSYS® and CFX® are registered trademarks of ANSYS, Inc. or its subsidiaries in the United States or other countries.

CFX® is a trademark of Sony Corporation in Japan.

Pointwise® is a registered trademark and Pointwise Glyph™ is a trademark of Pointwise Inc.

© Her Majesty the Queen in Right of Canada as represented by the Minister of National Defence, 2009

© Sa Majesté la Reine (en droit du Canada), telle que représentée par le ministre de la Défense nationale, 2009

Abstract

The evolution of laminar vortices was calculated using the Reynolds-averaged Navier-Stokes solver ANSYS CFX. Vortices of different strengths were modelled on unstructured grids using different element types and different node densities, then compared to an approximate solution of the Navier-Stokes equation. Grids using hexahedral or prismatic elements aligned with the vortex yielded significantly more accurate solutions than tetrahedral grids, especially when the circulating velocity was much smaller than the convection velocity. Over-diffusion of the circumferential velocity is the major source of error in these solutions.

ANSYS CFX was also used to determine the effect of grid density on a turbulent vortex, though in this case there is no analytic solution to compare with. As with the laminar vortex, grids using hexahedral or prismatic elements aligned with the vortex converge much more rapidly with cell size than tetrahedral grids, suggesting that they are more accurate. In these solutions the over-diffusion of turbulent viscosity by artificial viscosity is an important source of error.

The solutions are used to make recommendations for the density of unstructured grids required for accurate predictions of the pressure in the core as the vortex evolves over hundreds of core diameters.

Résumé

On a calculé l'évolution de tourbillons laminaires en utilisant le logiciel de résolution de l'équation de Navier-Stokes à moyenne de Reynolds ANSYS CFX. On a modélisé des tourbillons d'intensités différentes sur des maillages non structurés en utilisant différents types d'éléments et différentes densités nodales, puis en procédant à une comparaison avec une solution approximative de l'équation de Navier-Stokes. Les maillages à éléments hexaédraux prismatiques alignés avec le tourbillon ont donné des solutions nettement plus exactes que les maillages tétraédraux, particulièrement quand la vitesse de circulation était beaucoup plus petite que la vitesse de convection. La surdiffusion de la vitesse circonférentielle est la principale source d'erreur dans ces solutions.

On a également utilisé ANSYS CFX pour déterminer l'effet de la densité du maillage sur un tourbillon turbulent, bien qu'il n'y ait pas dans ce cas de solution analytique permettant de faire une comparaison. Comme avec le tourbillon laminaire, les maillages à éléments hexaédraux ou prismatiques alignés avec le tourbillon convergent beaucoup plus rapidement avec la taille des mailles que les maillages tétraédraux, ce qui porte à croire qu'ils sont plus précis. Dans ces solutions, la surdiffusion de la viscosité turbulente par la viscosité artificielle est une importante source d'erreur.

Les solutions sont utilisées pour faire des recommandations concernant la densité des maillages non structurés qui est requise pour obtenir des prévisions exactes de la pression au cœur du tourbillon quand celui-ci couvre des distances de l'ordre de plusieurs centaines de diamètres du cœur.

Executive summary

RANS calculations of the evolution of vortices on unstructured grids

David Hally; DRDC Atlantic TM 2009-052; Defence R&D Canada – Atlantic;
November 2009.

Background: The Maritime Asset Protection Section at DRDC Atlantic is applying Reynolds-averaged Navier-Stokes (RANS) flow solvers to predict the flow around ship propellers with the goal of being able to model the noise generated from propeller cavitation. Of particular interest is the cavitation in the vortex produced at the propeller tip. This form of cavitation is often the first to appear. It cannot be predicted by simpler flow solvers (panel methods) available at DRDC Atlantic.

In order to predict the cavitation, an accurate estimate of the pressure in the vortex core is needed. One question of interest is how dense the computational grid must be in the vortex core in order to model the pressure adequately. The answer will have an important effect on the gridding strategy used when preparing a propeller flow calculation. This report examines the effects of grid type and density on the predictions of the pressures in the cores of long rectilinear vortices.

Results: The evolution of laminar and turbulent vortices was calculated using the RANS solver ANSYS CFX from ANSYS, Inc. Vortices of different strengths were modelled on unstructured grids using different element types and different node densities. The solutions for laminar vortices were compared to an approximate solution of the Navier-Stokes equation.

It was found that significantly more accurate solutions were obtained when the grid cells were aligned with the direction of the vortex, especially when the circulating velocity was much smaller than the convection velocity. In particular, grids using only tetrahedra (in effect, no alignment with the flow at all) cause the vortex to dissipate rapidly unless very large numbers of cells are used.

Significance: These calculations indicate that although ANSYS CFX can predict vortex flows accurately using unstructured grids, the size of the grids may become very large for the calculation of propeller tip vortices. The estimates of minimum grid density will be used when formulating gridding strategies for vortices on propellers.

Future work: The calculations reported will be used to develop a strategy for generating grids capable of resolving propeller tip vortices adequately.

Sommaire

RANS calculations of the evolution of vortices on unstructured grids

David Hally ; DRDC Atlantic TM 2009-052 ; R & D pour la défense Canada – Atlantique ; novembre 2009.

Contexte : La Section de la protection des biens maritimes de RDDC Atlantique utilise des logiciels de résolution de l'équation de Navier-Stokes à moyenne de Reynolds (RANS) pour prévoir l'écoulement autour des hélices de navire dans le but de modéliser le bruit de la cavitation causé par les hélices. La cavitation dans le tourbillon créé à l'extrémité des hélices présente un intérêt particulier. Cette forme de cavitation est souvent la première à apparaître. Les logiciels de calcul d'écoulement (par la méthode de la plaque pleine) présentement disponibles à RDDC Atlantique ne permettent pas de la prévoir.

Une estimation exacte de la pression au cœur du tourbillon est nécessaire pour prévoir cette cavitation. L'une des questions à examiner est la densité que doit avoir le maillage de calcul dans le cœur du tourbillon pour que la pression soit modélisée de façon adéquate. La réponse aura une répercussion importante sur la stratégie de maillage utilisée dans le calcul de l'écoulement autour de l'hélice. Le présent rapport examine les effets du type et de la densité de maillage sur les prévisions de la pression au cœur de tourbillons rectilignes longs.

Résultats : On a calculé l'évolution de tourbillons laminaires et turbulents en utilisant le logiciel de résolution de l'équation de Navier-Stokes à moyenne de Reynolds ANSYS CFX de la société ANSYS Inc. On a modélisé des tourbillons d'intensités différentes sur des maillages non structurés en utilisant différents types d'éléments et différentes densités nodales. Les solutions pour les tourbillons laminaires ont été comparées à une solution approximative de l'équation de Navier-Stokes.

On a obtenu des solutions nettement plus exactes quand les mailles étaient alignées avec la direction du tourbillon, particulièrement quand la vitesse de circulation était beaucoup plus petite que la vitesse de convection. En particulier, à moins d'utiliser un grand nombre de mailles, les tourbillons subissent une dissipation rapide dans les maillages qui n'utilisent que des tétraèdres (absence totale d'alignement avec l'écoulement).

Importance : Ces calculs indiquent que, bien que le logiciel ANSYS CFX puisse prévoir les écoulements de tourbillons avec exactitude au moyen de maillages non

structurés, le nombre de mailles nécessaire peut devenir très grand pour le calcul des tourbillons à l'extrémité des hélices. On utilisera les estimations des densités minimales des maillages dans la formation des stratégies de maillage pour les tourbillons causés par les hélices.

Perspectives : Les calculs publiés seront utilisés pour élaborer une stratégie de génération de maillages permettant de calculer adéquatement les tourbillons aux extrémités des hélices.

This page intentionally left blank.

Table of contents

Abstract	i
Résumé	i
Executive summary	iii
Sommaire	iv
Table of contents	vii
List of figures	viii
1 Introduction	1
2 The evolution of a laminar vortex	1
2.1 Theory	1
2.2 RANS calculations	2
2.3 The hexahedral grids	3
2.4 The hybrid grids	4
2.5 The grids with prismatic elements	4
2.6 The grids with tetrahedral elements	6
2.7 Results of calculations	8
2.8 The effects of the discretization scheme for the convective terms	12
3 The evolution of a turbulent vortex	14
3.1 RANS calculations	14
3.2 Results of calculations	14
4 Implications for the gridding of propellers	17
5 Concluding remarks	20
References	21
Annex A: Results of the laminar computations	23
Annex B: Results of the turbulent computations	33
Annex C: Perturbation expansion of the vortex solution	43
List of symbols	51

List of figures

Figure 1:	The coordinate system	2
Figure 2:	The upstream face of the hexahedral grid (left) and the hybrid grid (right) with $N_c = 10$	5
Figure 3:	The upstream face of the prismatic and tetrahedral grids (right) with $N_c = 10$	5
Figure 4:	Laminar vortex: the pressure coefficient (left) and circumferential velocity (right) as a function of r/r_{ci} in the plane $x = x_{mid}$ with $\beta = 0.0446$	9
Figure 5:	Laminar vortex: the axial velocity deficit (left) and radial velocity (right) as a function of r/r_{ci} in the plane $x = x_{mid}$ with $\beta = 0.0446$	9
Figure 6:	Laminar vortex: the pressure coefficient (left) and axial velocity deficit (right) as a function of $(x - x_0)/r_{ci}$ on the centreline with $\beta = 0.0446$	9
Figure 7:	The pressure (left) and circumferential velocity v_θ (right) as a function of r in the plane $x = x_{mid}$	10
Figure 8:	The pressure (left) and circumferential velocity v_θ (right) as a function of r in the plane $x = x_{mid}$ when $\beta = 4.461$	11
Figure 9:	Comparison of the High Resolution Scheme and a fully second order accurate scheme on the prismatic and tetrahedral grids. . .	13
Figure 10:	The variation of the turbulent kinematic viscosity along the centreline for different values of the circulation.	15
Figure 11:	The propeller DTMB 4119: looking directly upstream (left) and from the side (right). The yellow circle marks the location of the data in Figure 12.	18
Figure 12:	The radial component (relative to the propeller axis) of the flow past DTMB 4119 along a circle passing through the vortex core. . .	18
Figure A.1:	Laminar vortex: the pressure coefficient (left) and circumferential velocity (right) as a function of r/r_{ci} in the plane $x = x_{mid}$ with $\beta = 0.0446$	24

Figure A.2:	Laminar vortex: the axial velocity deficit (left) and radial velocity (right) as a function of r/r_{ci} in the plane $x = x_{mid}$ with $\beta = 0.0446$.	25
Figure A.3:	Laminar vortex: the pressure coefficient (left) and axial velocity deficit (right) as a function of $(x - x_0)/r_{ci}$ on the centreline with $\beta = 0.0446$.	26
Figure A.4:	Laminar vortex: the pressure coefficient (left) and circumferential velocity (right) as a function of r/r_{ci} in the plane $x = x_{mid}$ with $\beta = 0.446$.	27
Figure A.5:	Laminar vortex: the axial velocity deficit (left) and radial velocity (right) as a function of r/r_{ci} in the plane $x = x_{mid}$ with $\beta = 0.446$.	28
Figure A.6:	Laminar vortex: the pressure coefficient (left) and axial velocity deficit (right) as a function of $(x - x_0)/r_{ci}$ on the centreline: $\beta = 0.446$.	29
Figure A.7:	Laminar vortex: the pressure coefficient (left) and circumferential velocity v_θ/U (right) as a function of r/r_{ci} in the plane $x = x_{mid}$ with $\beta = 4.461$.	30
Figure A.8:	Laminar vortex: the axial velocity deficit (left) and radial velocity (right) as a function of r/r_{ci} in the plane $x = x_{mid}$ with $\beta = 4.461$.	31
Figure A.9:	Laminar vortex: the pressure coefficient (left) and axial velocity deficit (right) as a function of $(x - x_0)/r_{ci}$ on the centreline: $\beta = 4.461$.	32
Figure B.1:	Turbulent vortex: the pressure coefficient (left) and circumferential velocity (right) as a function of r/r_{ci} in the plane $x = x_{mid}$ with $\beta = 0.0446$.	34
Figure B.2:	Turbulent vortex: the axial velocity deficit (left) and the turbulent viscosity (right) as a function of r/r_{ci} in the plane $x = x_{mid}$ with $\beta = 0.0446$.	35
Figure B.3:	Turbulent vortex: the pressure coefficient (left) and the turbulent viscosity (right) as a function of $(x - x_0)/r_{ci}$ on the centreline: $\beta = 0.0446$.	36

Figure B.4:	Turbulent vortex: the pressure coefficient (left) and circumferential velocity v_θ/U (right) as a function of r/r_{ci} in the plane $x = x_{mid}$ with $\beta = 0.446$	37
Figure B.5:	Turbulent vortex: the axial velocity deficit (left) and the turbulent viscosity (right) as a function of r/r_{ci} in the plane $x = x_{mid}$ with $\beta = 0.446$	38
Figure B.6:	Turbulent vortex: the pressure coefficient (left) and the turbulent viscosity (right) as a function of $(x - x_0)/r_{ci}$ on the centreline: $\beta = 0.446$	39
Figure B.7:	Turbulent vortex: the pressure coefficient (left) and circumferential velocity (right) as a function of r/r_{ci} in the plane $x = x_{mid}$ with $\beta = 4.461$	40
Figure B.8:	Turbulent vortex: the axial velocity deficit (left) and the turbulent viscosity (right) as a function of r/r_{ci} in the plane $x = x_{mid}$ with $\beta = 4.461$	41
Figure B.9:	Turbulent vortex: the pressure coefficient (left) and the turbulent viscosity (right) as a function of $(x - x_0)/r_{ci}$ on the centreline: $\beta = 4.461$	42

1 Introduction

The Maritime Asset Protection and the Warship Performance Sections at DRDC Atlantic apply Reynolds-averaged Navier-Stokes (RANS) solvers to the prediction of vortices generated by ships, submarines and propellers. Important applications are the prediction of tip and leading edge vortex cavitation on propellers, of keel and body vortices which can influence propeller efficiency and underwater vehicle maneuvering characteristics, and of low aspect ratio appendage wake vortices which can compromise the performance of downstream control surfaces (for example, the influence of a submarine sail on its tailplanes).

As a preliminary test, Hally and Watt[1] calculated the evolution of a laminar vortex on structured grids using the RANS solvers TRANSOM[2], developed at DRDC Atlantic, and CFX-TASCflow[3], developed by AEA Technology Ltd (now ANSYS, Inc.). There is an approximate solution to the Navier-Stokes equations which describes the vortex making it a good verification case for the flow solvers. This document describes similar calculations on unstructured grids using the RANS solver ANSYS CFX.

Four different types of grid were constructed using different combinations of hexahedral, prism and tetrahedral elements. Of interest is the effect of the grid density on the solution: for each type of grid, how many cells are necessary in the vortex core to model the pressure adequately? The dependence on the grid will have an important effect on the gridding strategy used when modelling propeller vortices. The dependence on grid density was tested using the laminar vortex as well as predictions of a turbulent vortex for which there is no analytical solution.

2 The evolution of a laminar vortex

2.1 Theory

In a convection dominated flow, in a cylindrical coordinate system (see Fig. 1), an approximate steady solution to the Navier-Stokes equations is:

$$v_x = U; \quad v_r = 0; \quad v_\theta = \frac{C}{2\pi r} (1 - e^{-z}); \quad p = -\frac{\rho C^2 U}{32\pi^2 \nu x} f(z) \quad (1)$$

where

$$z = \frac{r^2 U}{4\nu x}; \quad f(z) = \int_z^\infty \left(\frac{1 - e^{-y}}{y} \right)^2 dy \quad (2)$$

This is a vortex with centre on the line $r = 0$, circulation C , fluid density ρ and kinematic viscosity ν . The vortex decays as x increases. Annex C shows that the solution is a good approximation provided that

$$\nu \ll 0.2 r_c U; \quad \beta \ll 9 \quad (3)$$

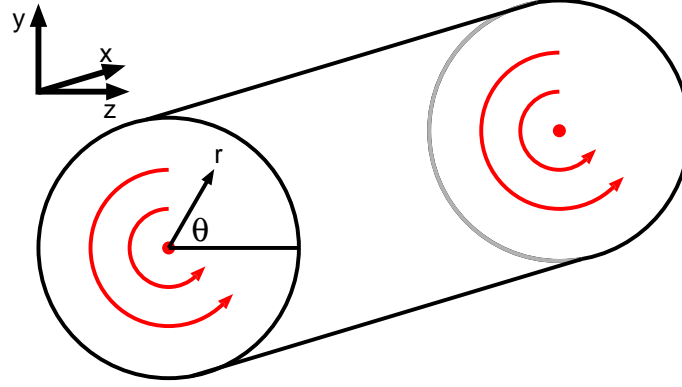


Figure 1: The coordinate system

where r_c is the radius of the vortex core, defined to be the location of maximum v_θ :

$$r_c \approx 2.24 \sqrt{\frac{\nu x}{U}} \quad (4)$$

and

$$\beta = \frac{C}{U r_{ci}} \quad (5)$$

with r_{ci} equal to r_c in the upstream plane. The parameter β is a non-dimensional measure of the strength of the vortex.

The maximum value of v_θ is

$$v_{\theta \max} \approx 0.114 \frac{C}{r_c} \quad (6)$$

More refined approximations for the axial and radial velocities, v_x and v_r , are given in [Annex C](#).

Eq. (4) implies that the core radius of r_{ci} will double to $2r_{ci}$ in a distance

$$L_r \approx \frac{1.6 U r_c^2}{\nu} \quad (7)$$

Over the same distance the maximum velocity drops by half and the pressure drop in the core decreases by one quarter.

2.2 RANS calculations

ANSYS CFX was used to calculate the evolution of a laminar vortex in water at standard temperature and pressure. In all cases the grid was bounded by a cylinder of radius $R = 20$ metres with axis extending from $x_0 = 1000$ metres to $x_1 = 2000$ metres.

The convection velocity was set by

$$U = \frac{\nu}{10^{-3}\text{m}} \quad (8)$$

and the circulation was set to $C = U \times 0.1\text{m}$, $U \times 1\text{m}$ or $U \times 10\text{m}$. The lowest value corresponds to the earlier calculations by Hally and Watt. The three values of C used in the calculations correspond to β values of 0.0446, 0.446 and 4.461.

The upstream plane was an inlet with velocity set using [Eq. \(1\)](#). The outer boundary was a free slip wall. The downstream plane was an outlet with average normal velocity set to U .

The ANSYS CFX “High Resolution Scheme” for discretization of the convection terms was used because it was felt that this would be the most practical scheme for the more complex flow around a propeller. The effect of this scheme relative to the second order accurate scheme is discussed in [Sec. 2.8](#).

Four different types of grid were used:

1. a structured grid consisting of hexahedra except for those elements along the centreline which were triangular prisms;
2. a hybrid grid with an inner portion using hexahedra and an outer portion using triangular prisms aligned with the flow;
3. a grid consisting of triangular prisms aligned with the flow; and
4. a grid consisting of tetrahedra.

For each grid type, calculations were made using five grids of differing node density near the vortex core. Each grid is described in detail in the following sections.

All the grids were generated using the scripting language Pointwise Glyph and the program Pointwise[\[4\]](#) from Pointwise, Inc.

2.3 The hexahedral grids

Let N_c be the number of nodes across the core of the vortex. The hexahedral grids had nodes of the form $\{(r_i, \theta_j, x_k) : i \in [1, N_r]; j \in [1, N_\theta]; k \in [1, N_x]\}$ with

$$\theta_j = \frac{2\pi(i-1)}{N_\theta - 1}; \quad x_k = x_0 + \frac{(k-1)(x_1 - x_0)}{N_x - 1} \quad (9)$$

In all cases $N_\theta = 64$ and $N_z = 101$. The r_i were calculated using a tanh distribution (see Hally[\[5\]](#)) with the spacing at $r = 0$ set to $s_0 = 2r_c/N_c$ and the spacing at $r = R$

set to $s_R = R/25$. The value of N_r was set so that the tanh distribution approximated a geometric distribution as closely as possible: i.e. the ratio of the cell sizes in the radial direction increased, as nearly as possible, in a geometric progression:

$$N_r = \left\lceil 1 + \frac{R \ln(s_R/s_0)}{s_R - s_0} \right\rceil \quad (10)$$

where $\lceil x \rceil$ denotes the closest integer to x .

The left side of Fig. 2 shows the grid on the upstream face of the cylinder for the case with $N_c = 10$.

2.4 The hybrid grids

The hybrid grids were generated by first making a hybrid grid on the upstream face of the cylinder. This grid was then extruded downstream using N_x translation steps parallel to the cylinder axis. With $N_x = 101$, this resulted in prismatic elements each of length 10 metres.

The hybrid grid on the upstream face was generated in three steps.

1. First a structured block two nodes deep was generated around the circumference of the cylinder. The purpose of this block was to improve the application of the CFX boundary conditions at the outer boundary.
2. Then a square structured block with sides of length $6r_c$ was created to cover the core of the vortex. The node separation in this block is r_c/N_c .
3. Finally an unstructured block was created in the region between the previous two blocks. The node separation increased gradually from the inner to the outer boundary.

The right side of Fig. 2 shows the grid on the upstream face of the cylinder for the case with $N_c = 10$.

2.5 The grids with prismatic elements

The grids with prismatic elements were generated by first making an unstructured grid on the upstream face of the cylinder. This grid was then extruded downstream in the same manner as the hybrid grids.

The unstructured grid on the upstream face was generated in a manner similar to the hybrid grids except that the inner block was an unstructured block of radius r_c with mean node separation r_c/N_c .

Fig. 3 shows the grid on the upstream face of the cylinder for the case with $N_c = 10$.

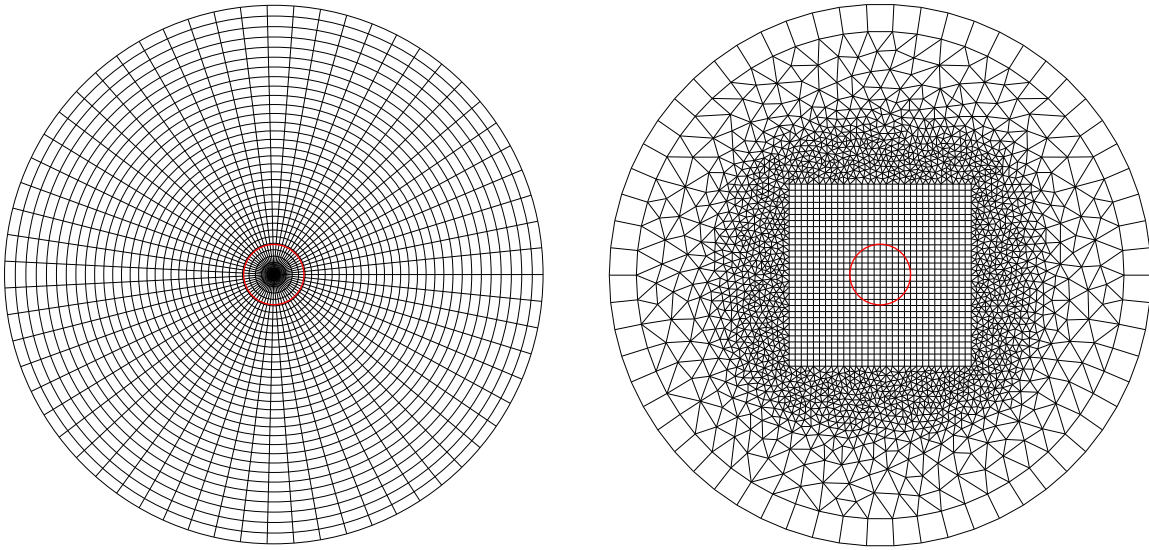


Figure 2: The upstream face of the hexahedral grid (left) and hybrid grid (right) with $N_c = 10$. The red circle marks the size of the vortex core.

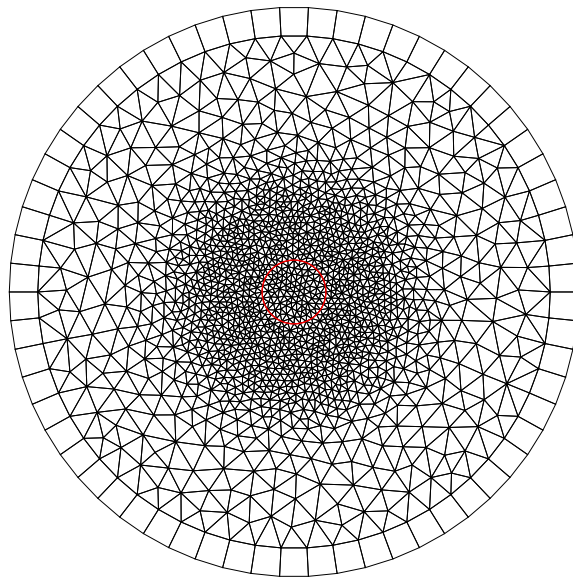


Figure 3: The upstream face of the prismatic and tetrahedral grids with $N_c = 10$. The red circle marks the size of the vortex core.

2.6 The grids with tetrahedral elements

The grids with tetrahedral elements were generated in four steps.

1. First a structured block two nodes deep was generated on the surface of the cylinder. As with the hybrid and prismatic grids, the purpose of this block was to improve the application of the CFX boundary conditions at the outer boundary.
2. An inner cylinder of radius r_c was generated and its surface gridded with a mesh of triangles with mean edge length of r_c/N_c .
3. The interior of the inner cylinder was gridded using tetrahedra with mean edge length of r_c/N_c .
4. The region between the inner cylinder and the outer structured block was gridded using tetrahedra whose edge lengths increased gradually with radius.

The grid on the upstream face of the tetrahedral grids is similar to that of the prismatic grids: see [Fig. 3](#).

It should be noted that the tetrahedral grids have far more elements than the hexahedral, hybrid or prismatic grids. This is because the tetrahedra have edges that are roughly uniform in size in all directions, while in the other two grids the edges aligned with the cylinder axis are much longer than the other edges. [Table 1](#) gives estimates of the number of nodes and elements for each of the grids as well as the number of nodes and elements in the vortex core. The latter two number increase roughly linearly with N_c for the hexahedral grids, quadratically with N_c for the hybrid and prismatic grids, and as N_c^3 for the tetrahedral grids.

Table 1: Estimates of the number of nodes and elements in each of the grids.

	N_c	No. Nodes total	No. Elements total	No. Nodes in core	No. Elements in core
Hexahedral	3	114,635	113,400	12,827	12,600
	6	165,539	163,800	19,190	18,900
	10	210,080	207,900	31,916	31,500
	16	254,621	252,000	51,005	50,400
	22	292,799	289,800	70,094	69,300
Hybrid	3	52,823	83,900	404	700
	6	122,513	197,600	2,727	2,800
	10	278,861	449,600	7,575	7,900
	16	644,986	1,034,200	19,695	20,100
	22	1,172,913	1,874,400	37,875	38,000
Prismatic	3	50,601	87,600	1,919	2,600
	6	80,497	146,800	4,343	6,600
	10	159,681	303,600	13,029	22,400
	16	316,635	614,400	24,947	44,200
	22	561,257	1,098,800	53,530	98,800
Tetrahedral	3	303,508	1,548,449	10,080	37,327
	6	484,929	2,645,971	51,014	232,517
	10	1,007,983	5,803,958	300,023	1,551,813
	16	2,057,450	12,136,019	948,935	5,134,227
	22	4,270,040	25,525,534	2,484,084	13,841,015

2.7 Results of calculations

It is important to note that the CFX boundary conditions are incapable of capturing the true conditions exactly at the upstream and downstream boundaries. Therefore, very close to the upstream and downstream planes the solutions exhibit higher errors than in the interior of the cylinder. To avoid the boundary effects we compare in a cross-stream plane at $x = x_{mid} = 1500$ metres, halfway along the cylinder. The results are also compared along the centreline of the vortex, $r = 0$.

Examples of the results for the prismatic grid with $\beta = 0.0446$ are shown in Figs. 4–6. Figs. 4 and 5 show the predicted values of pressure and circumferential velocity, v_θ , axial velocity deficit, $U - v_x$, and radial velocity, v_r , as a function of r/r_{ci} in the plane $x = x_{mid}$. Fig. 6 shows the pressure and axial velocity deficit as a function of $(x - x_0)/r_{ci}$ (i.e. the number of core radii downstream of the initial plane) along the centreline ($r = 0$). Similar plots for all grid types and values of β can be found in Annex A.

To generate Figs. 4 and 5, the results file from the calculation was loaded into the CFX post-processor, then interpolated to points in the plane $x = x_{mid}$, then written out to a data file. Each datum is shown by plotting its value (pressure or velocity component) versus the distance of the point from the axis. For the hexahedral grid (see Fig. A.1, for example), which exhibits complete axisymmetry, all the data for a single calculation should collapse to a line. However, for the unstructured grids in which the symmetry is broken, the data exhibit some spread.

In the figures, the solid black line shows the values predicted using Eq. (1) or by the refinements described in Annex C and given by Eqs. (C.33) and (C.60). When $\beta = 0.0446$ this provides an accurate estimate of the true solution; all numerical calculations should converge to the black line. When $\beta = 0.446$ (Figs. A.4–A.6), the approximations used in Eq. (1) are at the limits of their validity; all numerical calculations should converge close to the black line but small discrepancies should be expected within the vortex core. Also, as described above, for large r the axial velocity deficit $U - v_x$ is expected to be slightly negative due to the imposition of zero radial velocity on the outer boundary. When $\beta = 4.461$ (Figs. A.7–A.9), the approximations used in Eq. (1) are no longer valid; one should not expect the numerical predictions to converge to the black line; however, it is retained in the plots to make it easier to compare between the results at different circulations.

Because none of the boundary conditions used in the calculations (see Sec. 2.2) set a value for the pressure, the pressure is only defined relative to an unknown additive constant. To remove the ambiguity, the computed pressure values were offset so that the pressure at $(x, r, \theta) = (x_{mid}, R, 0)$ was equal to the theoretical value predicted by Eq. (1).

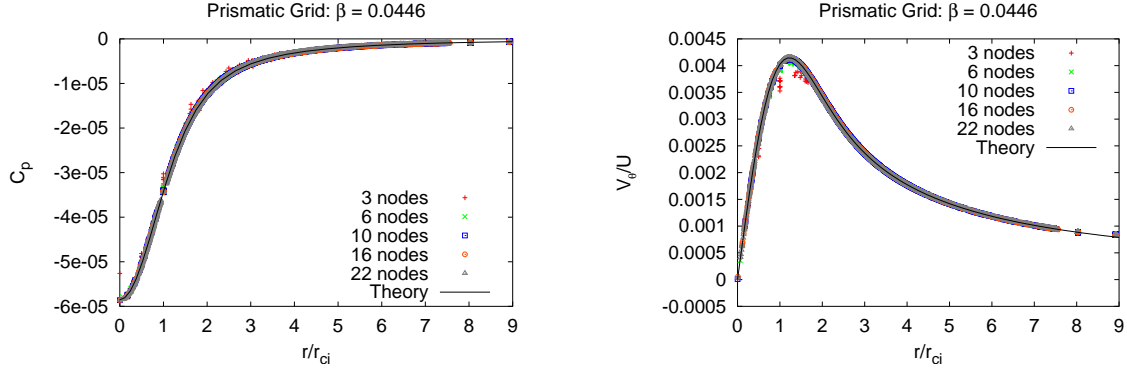


Figure 4: Laminar vortex: the pressure coefficient (left) and circumferential velocity (right) as a function of r/r_{ci} in the plane $x = x_{mid}$ with $\beta = 0.0446$.

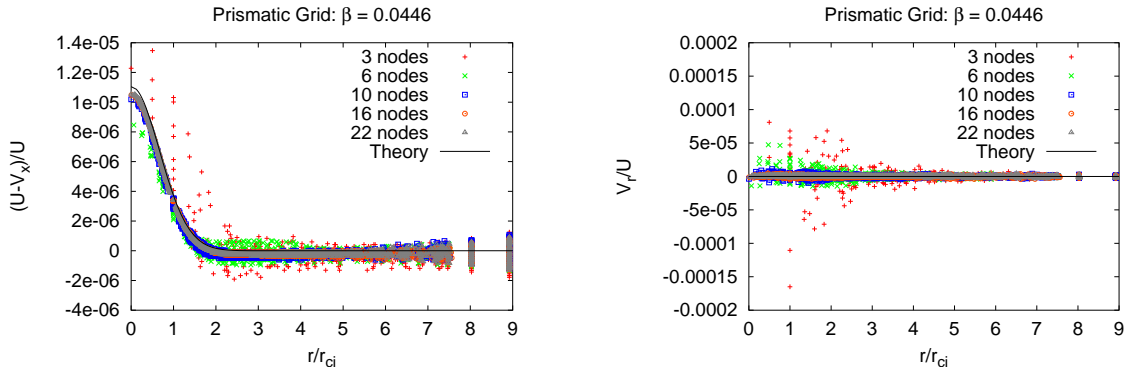


Figure 5: Laminar vortex: the axial velocity deficit (left) and radial velocity (right) as a function of r/r_{ci} in the plane $x = x_{mid}$ with $\beta = 0.0446$.

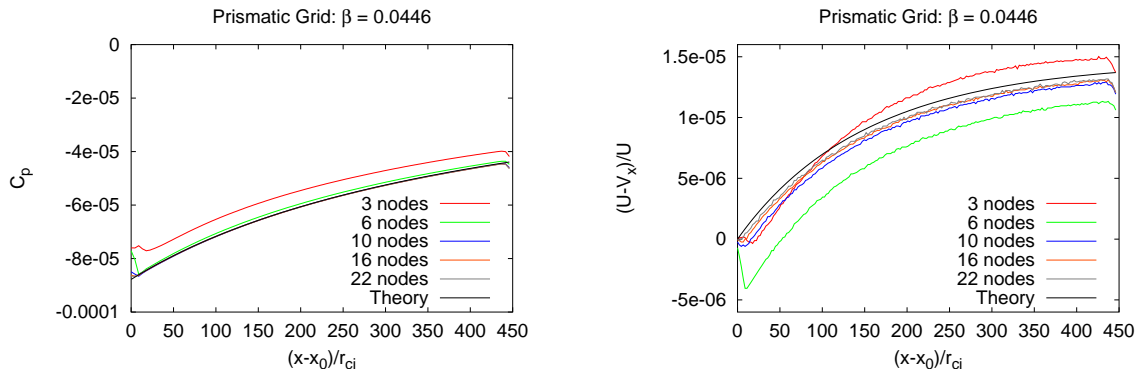


Figure 6: Laminar vortex: the pressure coefficient (left) and axial velocity deficit (right) as a function of $(x - x_0)/r_{ci}$ on the centreline with $\beta = 0.0446$.

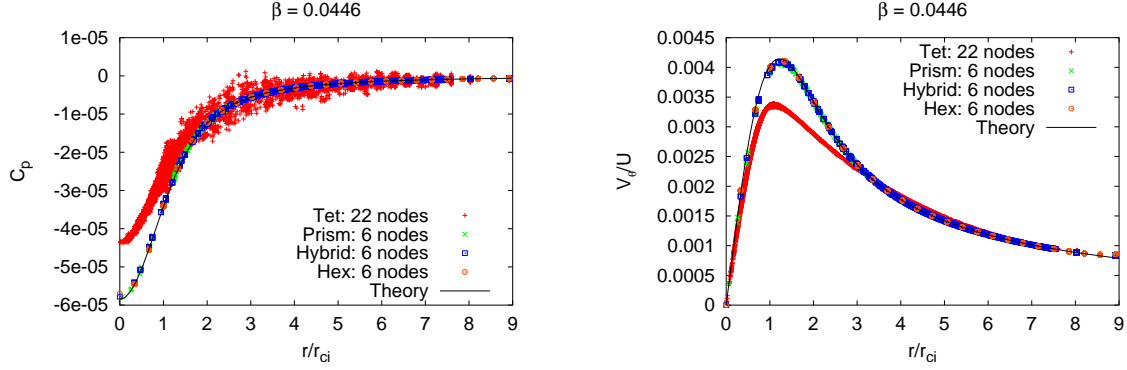


Figure 7: The pressure (left) and circumferential velocity v_θ (right) as a function of r in the plane $x = x_{mid}$.

Like the upstream and downstream boundaries, the free slip wall boundary condition used on the outer boundary is also not strictly accurate. In the theoretical solution the radial velocity at the outer boundary is small but positive. Therefore there is a small loss of fluid mass through the outer boundary which exactly compensates for the difference in fluid mass convected through the upstream and downstream boundaries due to the increase in axial velocity deficit. The axial velocity deficit in the theoretical solution rapidly approaches zero for large r . However, the free slip boundary condition requires that there be no flux of fluid through the outer boundary; therefore there is no loss of mass through the outer boundary and the mass convected through any cross stream plane must be constant. Therefore the integral of the axial velocity deficit over any cross stream plane must be zero. This causes a small negative shift of the calculated axial velocity; at large r the calculated axial velocity deficit approaches a small negative value, not zero.

The flow with $\beta = 0.0446$ corresponds to the tests run earlier by Hally and Watt. The current results for this flow are shown in Figs. A.1–A.3. For this case the hexahedral, hybrid and prismatic grids converge very well even when the number of nodes across the core is small. These results conform very closely to those reported for TRANSOM and CFX-TASCflow by Hally and Watt. However, when the tetrahedral grid is used the results are very poor; even with 22 nodes across the core the solution has not yet converged adequately. Fig. 7 shows the pressure and circumferential velocity predicted using the hexahedral, hybrid and prismatic grids with $N_c = 6$ and the tetrahedral grid with $N_c = 22$. The three former grids give much more accurate results despite the significantly smaller numbers of nodes.

The primary difference between the tetrahedral grid and the other three grid types is that the convection velocity, v_x , which is the dominant portion of the velocity field, is aligned with the faces of the prisms and hexahedra (i.e. it is either normal to or parallel to a face) while it is not aligned with the faces of the tetrahedra. This suggests

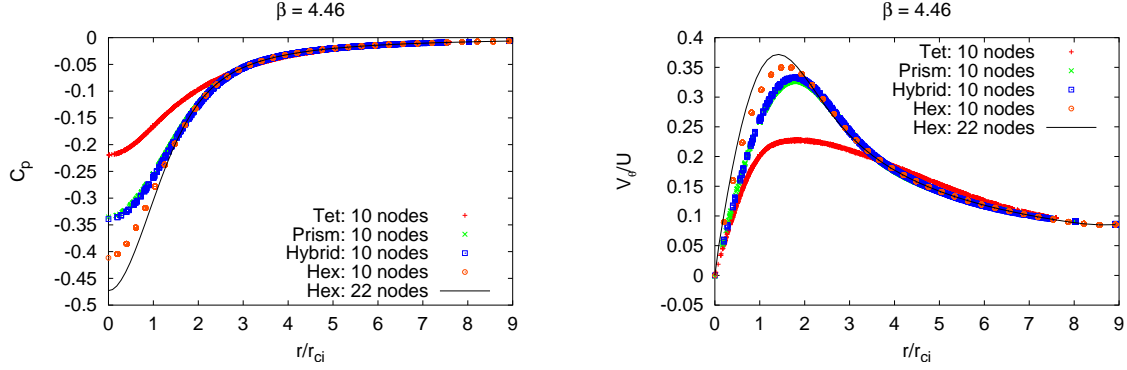


Figure 8: The pressure (left) and circumferential velocity v_θ (right) as a function of r in the plane $x = x_{mid}$ when $\beta = 4.461$.

that artificial viscosity is being introduced when the velocity crosses a face obliquely. Because $|v_x| \gg |v_\theta|$, the artificial viscosity induced by v_x significantly increases the effective viscosity causing v_θ and the pressure to be over-damped.

Notice that with the hexahedral grid the velocity v_θ is also aligned with the grid elements while this is not the case for the prismatic grid. Therefore, if the preceding hypothesis is correct, then the predictions with the prismatic grid should degrade as β is increased, thus increasing the relative importance of v_θ . That this is the case can be seen from Figs. A.4–A.9 which show the predictions with the circulation parameter β set to 0.446 and 4.461. As β is increased, the predictions using the hexahedral grids are the best, then those of the hybrid and prismatic grids, then those of the tetrahedral grids. The tetrahedral grids degrade the least as β is increased, but only because their predictions were so poor for the smallest value of β . Fig. 8 also shows the relative accuracy of the four grid types when the circulation is large. It compares the pressure and circumferential velocity predicted using the four grid types with $N_c = 10$ and $\beta = 4.461$. For comparison, the prediction using the hexahedral grid with $N_c = 22$ is also shown; it is close to the true solution.

To check the adequacy of the resolution in the x direction of the hexahedral, hybrid and prismatic grids, calculations were made using $N_c = 22$ but with $N_x = 201$ and 401. The difference in the calculated pressures and velocities is barely discernible when plotted. They are not shown here.

The calculations on the tetrahedral grid are consistent with an artificial viscosity caused by the discretization of x -momentum of

$$\nu_{x,art} \approx 0.01 \frac{U r_c}{N_c} = 0.005 U \Delta. \quad (11)$$

where $\Delta = 2r_c/N_c$ is the size of the cells in the core. For an accurate solution the artificial viscosity must be significantly smaller than the kinematic viscosity, ν .

Therefore,

$$N_c \gg \frac{0.01Ur_c}{\nu}; \quad \Delta \ll 200\frac{\nu}{U} \quad (12)$$

which, for the cases described here, requires that $N_c \gg 22$.

When β is large, the discretization of circumferential momentum also induces significant artificial viscosity on the tetrahedral, prismatic and hybrid grids. In that case:

$$\nu_{\theta,art} \approx 0.01 \frac{r_c v_{\theta max}}{N_c} \approx \frac{0.001C}{N_c} = \frac{0.0005C\Delta}{r_c} = 0.0005\beta U \Delta. \quad (13)$$

For accurate solutions one then needs

$$N_c \gg 0.001 \frac{C}{\nu} = 0.001 \frac{\beta U r_{ci}}{\nu}; \quad \Delta \ll \frac{2000\nu r_c}{C} = \frac{2000\nu}{\beta U} \quad (14)$$

which for the cases described here requires that $N_c \gg 2.2\beta$.

From Eqs. (11) and (13), $\nu_{x,art} = \nu_{\theta,art}$ when $\beta = 10$ which suggests that the hybrid, prismatic and tetrahedral grids should have similar accuracy when $\beta > 10$, but that the hybrid and prismatic grids will be more accurate for smaller β .

2.8 The effects of the discretization scheme for the convective terms

The calculations shown in Annexes A and B were calculated using the ANSYS CFX “High Resolution Scheme” for discretization of the convection terms in the equations of motion. This scheme is a blend of a second order accurate scheme and a first order accurate upwind differencing scheme. The blend factor is calculated locally so the scheme is as close to second order accurate as possible without introducing local oscillations [6].

It is natural to assume that some of the high diffusivity exhibited by the solutions on the tetrahedral grid is attributable to the first order component of the the High Resolution Scheme. Therefore all the laminar calculations on the tetrahedral grid were repeated using a fully second order accurate scheme. Some of the calculations on the other grids were also repeated. Fig. 9 compares the results of the two different discretization schemes for the case with $\beta = 0.446$ and $N_c = 10$ on the prismatic and tetrahedral grids. The results on the prismatic grid show very little change with the discretization scheme: so much so that it is often difficult to discern the symbols for the High Resolution Scheme as they are overlaid by the symbols from the second order accurate scheme. There is more variation with the tetrahedral grid but, counterintuitively, the second order scheme increases the diffusivity causing poorer accuracy relative to the theoretical curves. Only the radial component of

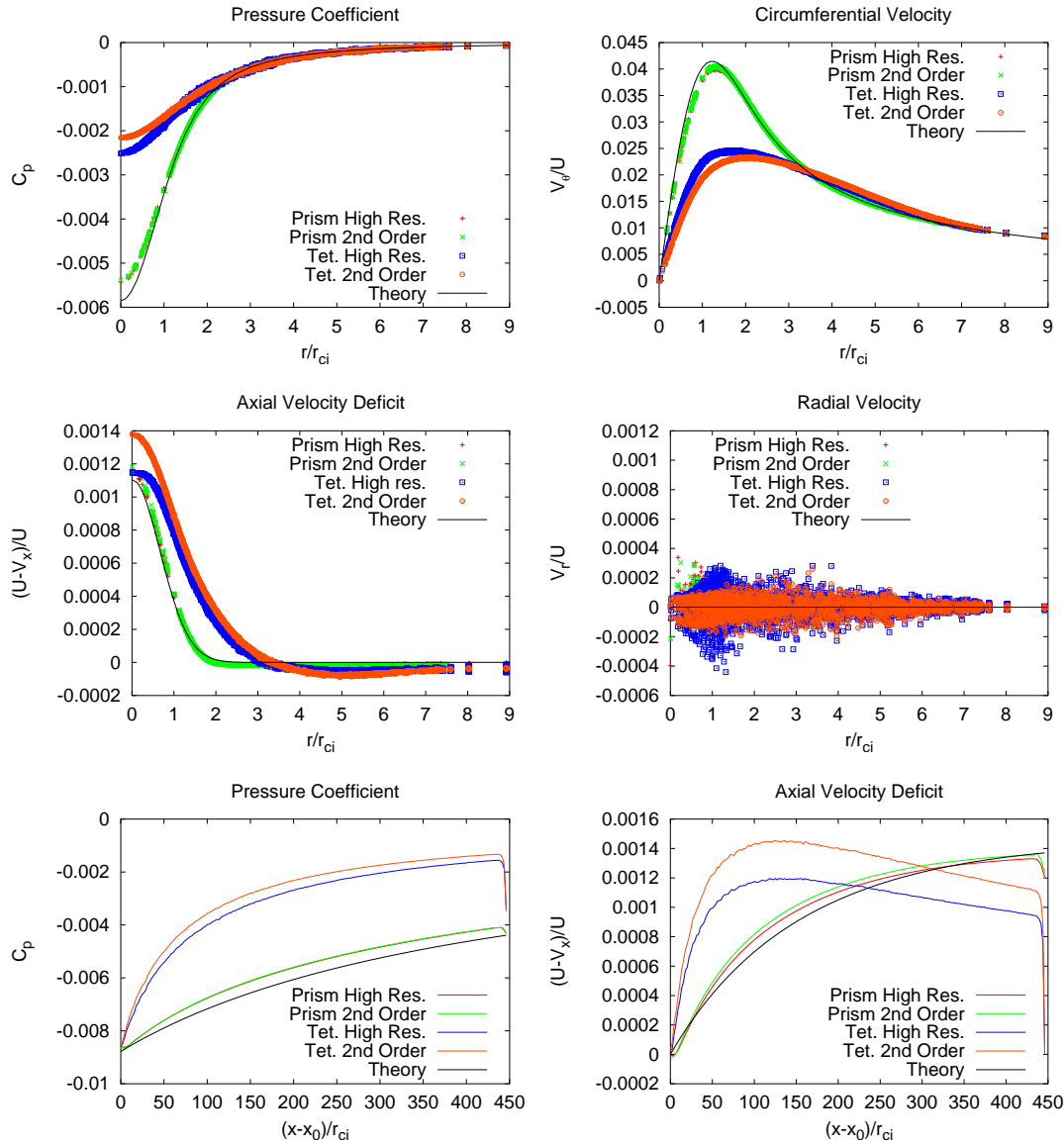


Figure 9: Comparison of the High Resolution Scheme and a fully second order accurate scheme on the prismatic and tetrahedral grids: $\beta = 0.446$, $N_c = 10$. The top four figures plot pressure coefficient, circumferential velocity, axial velocity deficit and radial velocity as a function of r/r_{ci} in the midstream plane, $x = x_{mid}$. The bottom two figures plot pressure coefficient and axial velocity deficit along the centreline.

the velocity shows a slight improvement with less scatter when the High resolution Scheme is used. These results are consistent across all the cases tried: the hexahedral, prismatic and hybrid grids are insensitive to the discretization; the tetrahedral grid is more sensitive to the scheme used and the second order scheme is more diffusive. We do not understand why the second order scheme is more diffusive.

3 The evolution of a turbulent vortex

3.1 RANS calculations

ANSYS CFX was used to calculate the evolution of turbulent vortices in water at a standard temperature and pressure. The same grids were used as in the laminar calculations. The upstream plane was an inlet with velocity set using Eq. (1) with $U = 1$ m/sec. Three values for the circulation were used, set so that their non-dimensional values were the same as for the laminar case: $\beta = 0.0446, 0.446$ and 4.461 . The outer boundary was a free slip wall. The downstream plane was an outlet with average normal velocity set to U . In the upstream plane the turbulent kinetic energy was set to

$$k = \frac{3}{2}IU^2; \quad I = 0.001 + 0.01e^{-(r/r_{ci})^2} \quad (15)$$

and the eddy viscosity ratio to

$$\frac{\nu_t}{\nu} = 1 + 1000e^{-(r/r_{ci})^2} \quad (16)$$

Since the default kinematic viscosity of water used by ANSYS CFX is 8.926×10^{-7} m²/sec, the maximum value of $\nu_t/U r_{ci}$ in the initial plane is 3.98×10^{-4} , close to the value of $\nu/U r_{ci}$ for the laminar runs (4.46×10^{-4}). However, in the turbulent case ν_t is confined within the vortex core and evolves with the flow.

The Shear Stress Transport (SST) turbulence model was used for all turbulent calculations.

3.2 Results of calculations

Annex B contains figures showing the results of the turbulent calculations on all the grids for flows with $\beta = 0.0446, 0.446$ and 4.461 . The predicted values of pressure coefficient, C_p , circumferential velocity, v_θ/U , axial velocity deficit, $(U - v_x)/U$, and $\nu_t/U r_{ci}$, are plotted as a function of r/r_{ci} in the plane $x = x_{mid}$. The pressure and turbulent viscosity are also plotted as a function of $(x - x_0)/r_{ci}$ along the centreline ($r = 0$).

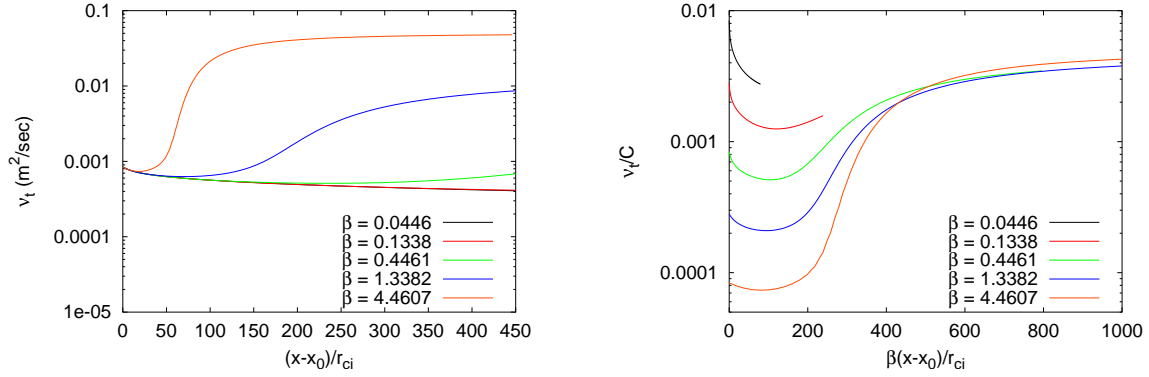


Figure 10: The variation of the turbulent kinematic viscosity along the centreline for different values of the circulation. On the left the data is plotted as ν_t vs. $(x - x_0)/r_{ci}$; on the right it is plotted as ν_t/C vs. $\beta(x - x_0)/r_{ci}$.

The only significant difference in the way the laminar and viscous calculations were set up is in the kinematic viscosity. Therefore we first consider how it changes as the vortex evolves.

In a turbulent vortex, if the turbulent viscosity is significantly higher than the laminar viscosity, then in the cross-stream plane, in which the flow is largely decoupled from the flow in the downstream direction, there are only two dimensional parameters of significance: the circulation, C , and the core radius, r_c . This implies that the turbulent viscosity will be roughly proportional to C : $\nu_t \approx \alpha C$. If ν_t is too high, the turbulent viscosity diffuses radially, smearing itself over a larger area until its diffusion is just matched by its production; if it is too low, production will dominate diffusion, increasing the turbulent viscosity until diffusion and production are balanced.

In practice, when the turbulent viscosity is initially smaller than αC , it may take a long time before it increases to the point where diffusion balances production. The time scale over which it increases is proportional to the inverse of the mean strain. Since the mean strain is proportional to $C/r_c^2 = \beta U/r_c$, the time scale is inversely proportional to β ; weaker vortices take longer to evolve. Put another way, the distance traversed before the core begins its rapid production of turbulent viscosity is proportional to β .

The left side of Fig. 10 shows the turbulent kinematic viscosity along the centreline for three different values of β on the hexahedral grid with 22 nodes across the core (extra calculations were done to include the intermediate β values of 0.1338 and 1.338). The calculations were performed using the hexahedral grid with 22 nodes across the core. When $\beta = 4.461$, after a small initial decrease, the turbulent viscosity increases very rapidly at about 50 core radii downstream of the initial plane; for $\beta = 1.338$ the rapid increase is delayed until about 150 core radii; for $\beta = 0.446$ the viscosity is only just

beginning to increase at 450 core radii. At the two lower values of β the viscosity continues to decrease for 450 core radii.

The right side of Fig. 10 shows the same data as the left side but with ν_t/C plotted against $\beta(x - x_0)/r_{ci}$. (Additional calculations were required to make this figure, both at the intermediate values of β and on a grid elongated to $x_1 = 5000$ metres. Even so the curves at the lower values of β are truncated because the grid was not long enough.) Despite the differing values of ν_t/C at the initial plane, for each value of C the rapid production of vorticity begins near $\beta(x - x_0)/r_{ci} = 200$. Moreover, after the rapid production the value of ν_t/C appear to be approaching a constant value, α , near 0.004, though this is uncertain for the lower values of β for which the curves are truncated.

The value of α at which production matches diffusion is, in the computer codes, dependent on the turbulence model used. It is well known that isotropic turbulence models tend to overpredict the production of turbulent viscosity in vortices; therefore the value of 0.004 suggested by these results for the SST model is expected to be higher than the values predicted by non-isotropic models.

Once diffusion and production are matched, the viscosity is roughly constant and we can expect it to evolve roughly as a laminar vortex. Therefore, from Eq. (7), its core radius will double in a distance

$$L_r \approx \frac{1.6U_r^2}{\nu_t} \approx \frac{1.6r_c}{\alpha\beta} \quad (17)$$

and over the same distance the maximum velocity will reduce by half and the pressure drop will decrease to one quarter of its value. For values of β near 1.0, L_r is a few hundred core radii. For smaller values of β it can be thousands of core radii.

For the lowest value of β in the numerical calculations, the initial value of ν_t exceeds αC . Therefore the viscosity is reduced by self-diffusion resulting in a vortex whose effective Reynolds number, Ur_c/ν_t , is larger than for the laminar case. Therefore we can expect the results on the tetrahedral grid to be very poor, the turbulent viscosity being completely masked by artificial viscosity. Figs. B.1–B.3 show this to be true. Moreover, as can be seen in the lower right graphs of Figs. B.2 and B.3, the artificial viscosity diffuses the turbulent viscosity so much that it is effectively removed. On the other hand, the other three grids all give very accurate results for this case, converging well, as in the laminar case, with only a few nodes across the core.

When the strength of the vortex is increased to $\beta = 0.446$ (Figs. B.4–B.6), the initial value of ν_t is significantly smaller αC , so that it will eventually increase. From Fig. B.6 we can see that at the mid-plane the increase is just beginning. The graphs on the right of Fig. B.5 show that viscosity is being produced near the location of peak

velocity where the mean strain is highest. For this value of β the trends with varying number of nodes are again similar to the laminar case: the hexahedral grid converges very well, the hybrid and prismatic grids are similar but not quite as good as the hexahedral grid, and the tetrahedral grid is still very poor.

When the strength of the vortex is increased further to $\beta = 4.461$ (Figs. B.7–B.9) the flow in the mid-plane is significantly different from the cases with lower β . Now the vorticity has already undergone the major portion of its increase and is approaching its final state as a well-developed vortex. An interesting feature of the flow is that increasing the node density now results in lower maximum velocities and smaller pressure drops in the core. The reason for this can be found in Fig. B.9. When the node density is lower, increased artificial viscosity results in greater diffusion of the velocity in the early stages of evolution. The mean strain is then lower and the rapid increase of vorticity is delayed. As a result the vortex does not diffuse as much and the maximum velocity is higher.

Judging the convergence characteristics from Figs. B.7–B.8, it is difficult to choose between the three non-tetrahedral grids, but Fig. B.9 once again shows that the hexahedral grid is best and the hybrid and prismatic grids are somewhat poorer. As always the tetrahedral grid ranks last.

4 Implications for the gridding of propellers

The flow past propeller DTMB 4119, shown in Fig. 11, has been studied experimentally by Jessup et al.[7,8] and was used as a test case by the 22nd ITTC Propulsion Committee Propeller RANS/Panel Method Workshop in Grenoble, 1998.

Let V be the speed of advance of the propeller and let V_r be the component of the fluid velocity pointing radially outward from the propeller axis. Fig. 12 plots measured values of V_r/V for DTMB 4119 on a circle just downstream of the propeller blades, centred on the propeller axis and passing through the core of the tip vortices. The location of the circle is shown in Fig. 11. As this is a three-bladed propeller, V_r is only plotted along one third of the circle. The core of the vortex is easily identified as the region between the maximum and minimum values of V_r , a region with angular extent of about 4 degrees. As the circle has a radius of $r = 0.924R$, this represents a distance of about $0.065R$, where R is the propeller radius. However, the vortex cuts through the plane of the circle obliquely causing the vortex to be stretched by the factor $\sqrt{1 + (\pi r/JR)^2}$ in the direction tangent to the circle. Since the advance ratio $J = 0.833$, this means that the actual diameter of the core is about 3.6 times smaller than the distance on the plot: i.e. $r_c \approx 0.009R$.

The vortex strength, β , can also be estimated from the difference in value of the

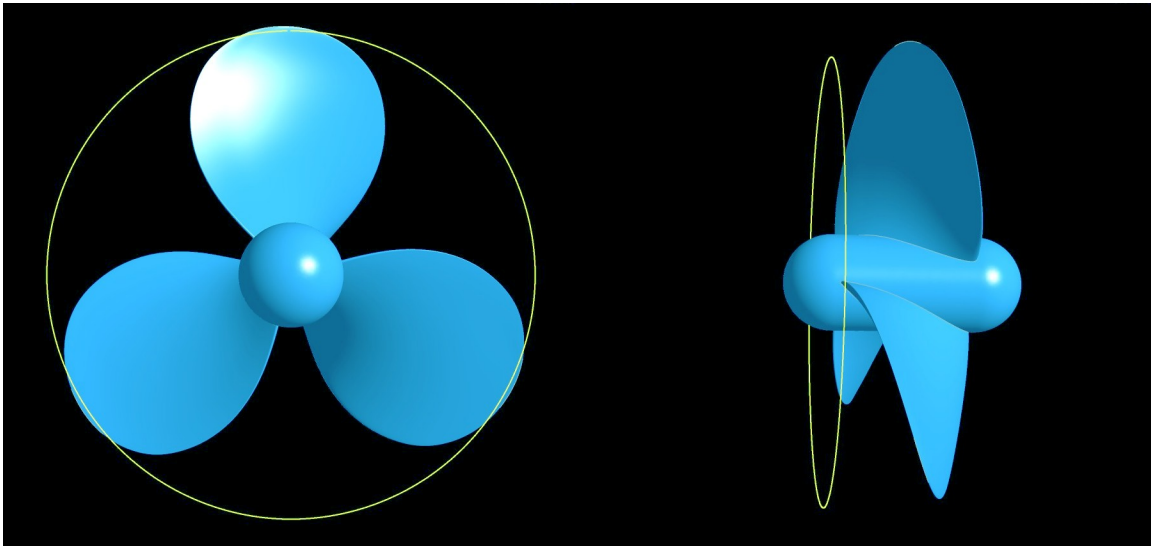


Figure 11: The propeller DTMB 4119: looking directly upstream (left) and from the side (right). The yellow circle marks the location of the data in Figure 12.

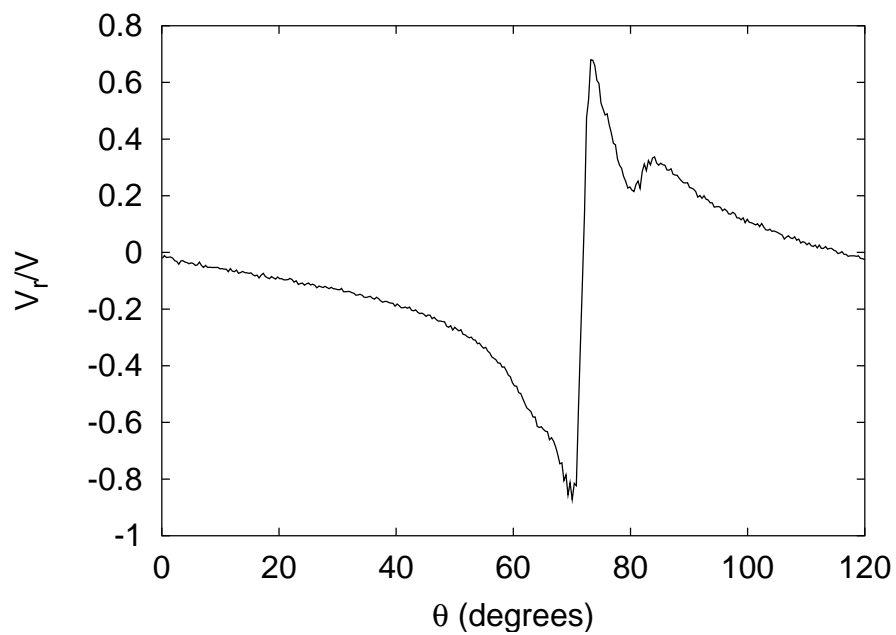


Figure 12: The radial component (relative to the propeller axis) of the flow past DTMB 4119 along a circle passing through the vortex core.

minimum and maximum of V_r and Eq. (6). Note that the convection speed, U , is the combination of the inflow speed, V , and the velocity induced by the propeller rotation: $U = V\sqrt{1 + (\pi r/JR)^2} \approx 3.6V$. Therefore

$$v_{\theta max} \approx \frac{\Delta V_r}{2} \approx 0.776V; \quad \beta = \frac{C}{U r_c} \approx \frac{v_{\theta max}}{0.114U} \approx 6.8 \frac{V}{U} \approx 1.9 \quad (18)$$

Since $V = 2.54$ m/sec and the propeller radius is 152.4 mm, the circulation can be estimated as $C = 2.4 \times 10^{-2}$ m²/sec and the limiting value of the turbulent viscosity once the vortex is well-developed will be about $\nu_t \approx 0.004C \approx 10^{-4}$ m²/sec. Thereafter the maximum radius will decrease by half over a distance of roughly $2R$ or about one third of a turn of the propeller.

Fig. 10 suggests that the vortex will evolve slowly for about 100 core radii before the vorticity increases sufficiently that it diffuses quickly. What is the best way to construct the grid if we wish to predict the vortex characteristics accurately over this distance?

A tetrahedral grid is easiest to generate, but it will require a minimum of 20 nodes across the core which gives about 600,000 nodes just within the core of a single vortex. Moreover, DTMB 4119 is a model scale propeller; for propellers at full scale the vortex core is expected to be even smaller. Therefore, even if grid adaptation is used to refine the grid near the vortex cores, very large grids will be required.

Although the numerical tests suggest that a hexahedral grid yields the best accuracy for the fewest number of nodes, that is really only because the grid is perfectly centred on the vortex. As soon as the vortex core moves away from the centre of the grid, the velocity components cross the element faces obliquely and the hexahedral grids give results similar to the prismatic grid. Therefore the location of the vortex would need to be known very accurately if the benefits of the hexahedral grid are to be obtained. Moreover, the upstream and downstream faces of the hexahedral grids contain very thin triangular elements. These make it hard to embed a hexahedral grid within a larger unstructured grid covering the remainder of the fluid. Therefore, the hexahedral grid is not a practical option.

On the other hand, only a reasonable estimate of the locations of the vortex cores is necessary to get adequate alignment of the hybrid or prismatic grids. Such estimates are easily obtained from actuator disk theory once the thrust is known. These grids offer the prospect of a considerable reduction in the number of nodes, both because somewhat fewer nodes are required across the core to get similar accuracy, and because the elements can be elongated along the direction of the vortex. Moreover, there is no difficulty in embedding a hybrid or prismatic grid enclosing the vortex within a larger unstructured grid. Therefore these grid types are the most attractive option. A simple gridding procedure would be to calculate the flow on an initial grid to estimate

the thrust, then generate a new grid with prismatic refinement along the vortex cores. One can easily envisage further iterations of the grid as the vortex locations become known more accurately with each set of calculations.

5 Concluding remarks

The evolution of laminar and turbulent rectilinear vortices has been studied using the flow solver ANSYS CFX. The results confirm the finding of an earlier study by Hally and Watt [1] that accurate predictions of weak laminar vortices ($\beta \ll 1$) over distances equal to hundreds of core radii can be attained with 6 to 10 nodes across the core. However, good predictions can only be obtained if the grid is comprised of hexahedral or prismatic elements whose faces are either aligned with, or perpendicular to, the vortex axis. In cases in which the faces cut the vortex at large oblique angles, in particular a tetrahedral grid, artificial dissipation induced by the convection velocity across the faces results in excessive dissipation and poor predictions.

The current study also examined strong laminar vortices with β of the order of 1 or greater. For many practical flows, including propeller tip vortices, this is a more realistic range of values. In a strong vortex the circumferential velocity is similar in magnitude to the convection velocity and the artificial dissipation caused by the circumferential velocity crossing oblique faces in the grid becomes an important factor. Therefore, even when the element faces are aligned with the vortex axis, larger numbers of nodes are needed to reduce the artificial dissipation to acceptable levels: when $\beta = 0.446$, approximately 16 nodes across the core and, when $\beta = 4.446$, more than 22 nodes across the core to get similar accuracy as 6 nodes across the core when $\beta = 0.0446$. Nevertheless, one still finds that there is a significant improvement when the grids are aligned (the hexahedral, hybrid and prismatic grids) than when they are not (the tetrahedral grid).

When the vortex is turbulent, it will evolve towards a well-developed state in which the turbulent vorticity is proportional to the circulation. Therefore weak vortices will have low levels of vorticity and will consequently evolve slowly. The effects of the grid on the flow predictions are similar to those of the laminar case. When the vortex is strong, an initial low level of vorticity will increase towards its final state; the stronger the vortex, the more rapidly the vortex will reach its fully-developed state. In these cases artificial viscosity can have an important effect in reducing the mean strain that drives the production of vorticity; therefore, coarse grids overestimate the time taken to achieve the well-developed state.

References

- [1] Hally, D. and Watt, G. D. (2001), RANS calculations of the evolution of vortices, (DREA TR 2001-216) Defence R&D Canada – Atlantic.
- [2] Hally, D. (1997), TRANSOM: A Multi-method Navier-Stokes Solver: Overall Design, (DREA TM 97-231) Defence R&D Canada – Atlantic.
- [3] CFX-TASCflow (online), AEA Technology Ltd,
<http://www.software.aeat.com/cfx/products/cfx-tascflow> (Access Date: Apr. 2002).
- [4] (2008), Pointwise: Reliable CFD Meshing You Trust (online), Pointwise, Inc., Fort Worth, Texas, <http://www.pointwise.com> (Access Date: November 2008).
- [5] Hally, D. (2006), C++ classes for representing curves and surfaces: Part IV: Distribution functions, (DRDC Atlantic TM 2006-257) Defence R&D Canada – Atlantic.
- [6] (2006), ANSYS CFX Solver Theory Guide: Discretization and Solution Theory: Numerical Discretization, ANSYS, Inc.
- [7] Jessup, S. D. (1989), An Experimental Investigation of Viscous Aspects of Propeller Blade Flow, Ph.D. thesis, School of Engineering and Architecture, The Catholic University of America.
- [8] Jessup, S. D. (1998), Experimental data for RANS calculations and comparisons (DTMB4119), In *Proceedings of Propeller RANS/Panel Method Workshop*, 22nd ITTC Propulsion Committee, Grenoble, France.

This page intentionally left blank.

Annex A: Results of the laminar computations

The figures on the following pages show the results of the laminar computations for each type of grid. For each grid and for each value of the parameter β , six plots are presented:

1. the pressure coefficient as a function of r/r_{ci} in the plane $x = x_{mid}$;
2. the circumferential velocity, v_θ/U , as a function of r/r_{ci} in the plane $x = x_{mid}$;
3. the axial velocity deficit, $(U - v_x)/U$, as a function of r/r_{ci} in the plane $x = x_{mid}$;
4. the radial velocity, v_r/U , as a function of r/r_{ci} in the plane $x = x_{mid}$;
5. the pressure coefficient along the centreline as a function of the distance from the initial plane measured in core radii (i.e. $(x - x_0)/r_{ci}$); and
6. the axial velocity deficit, $(U - v_x)/U$, along the centreline as a function of the distance from the initial plane measured in core radii.

Each plot shows the results for six runs with varying numbers of nodes across the vortex core.

For easy comparison between the different grids, the results for each of the three grid types are shown on the same page.

In all the figures, the solid black line shows the values predicted using Eq. (1). When $\beta = 0.0446$ this provides an accurate estimate of the true solution; all numerical calculations should converge to the black line. When $\beta = 0.446$, the approximations used in Eq. (1) are at the limits of their validity; all numerical calculations should converge close to the black line but small discrepancies should be expected within the vortex core. When $\beta = 4.461$, the approximations used in Eq. (1) are no longer valid; one should not expect the numerical predictions to converge to the black line; however, it is retained in the plots to make it easier to compare between the results at different circulations.

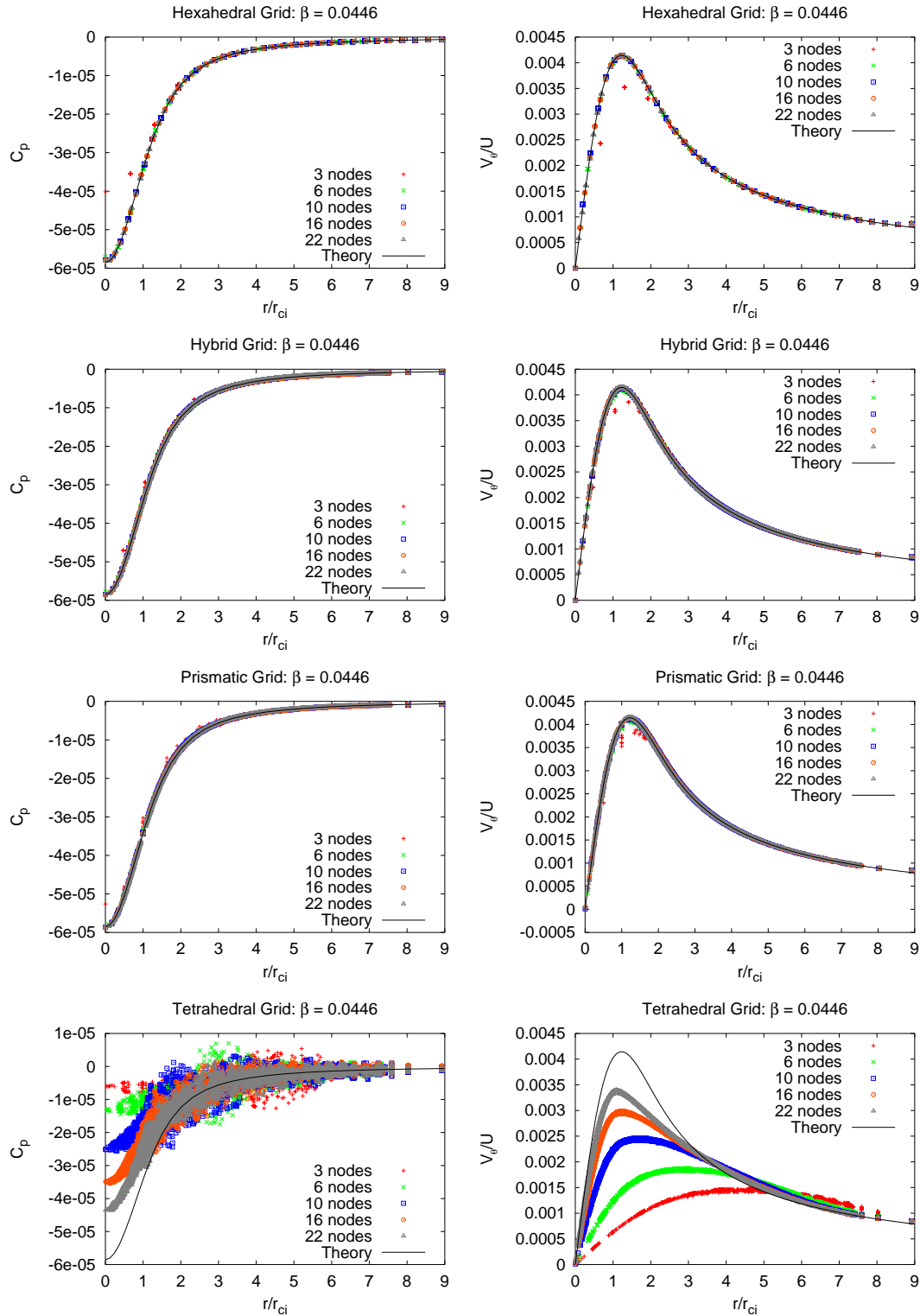


Figure A.1: Laminar vortex: the pressure coefficient (left) and circumferential velocity (right) as a function of r/r_{ci} in the plane $x = x_{mid}$ with $\beta = 0.0446$.

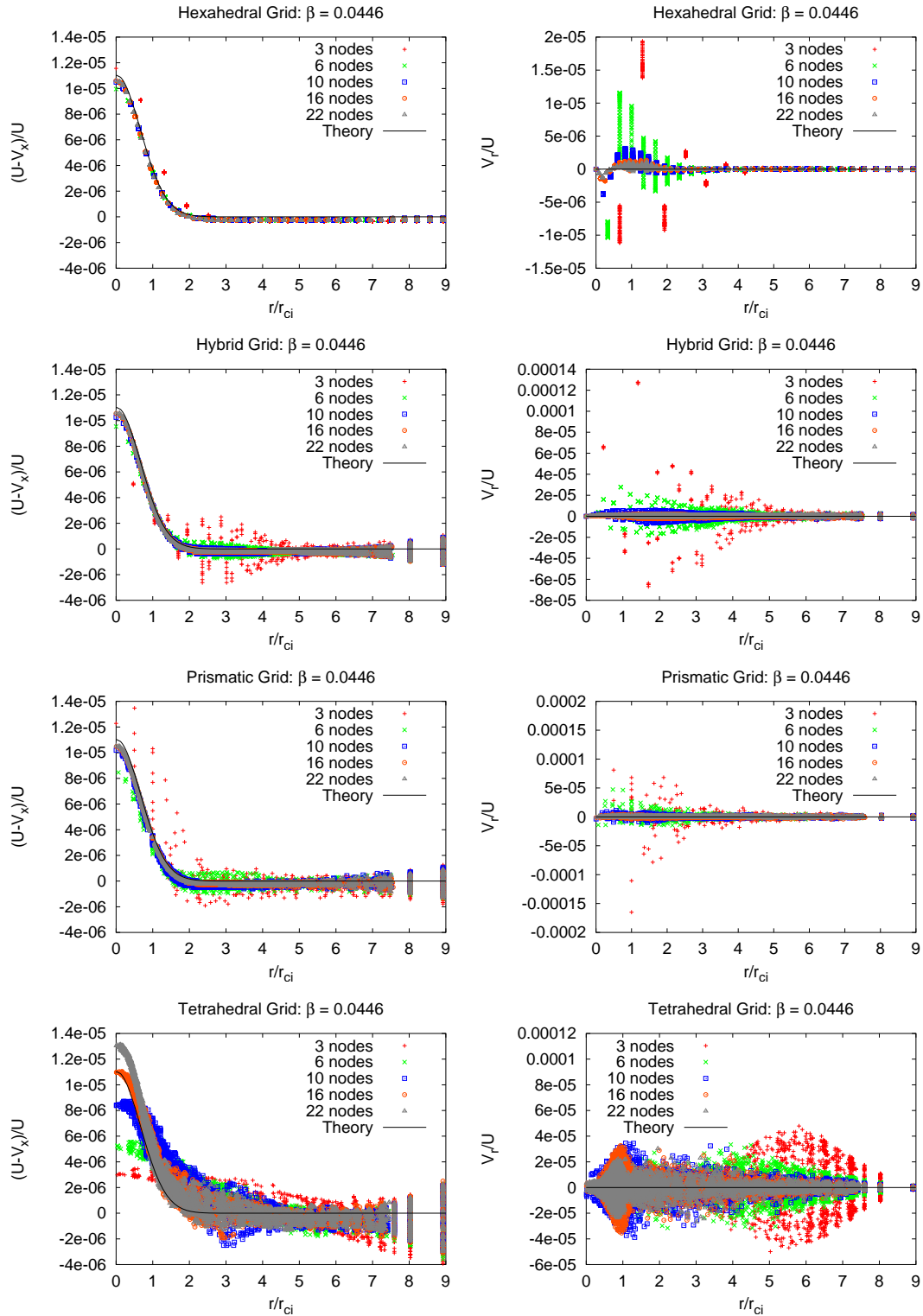


Figure A.2: Laminar vortex: the axial velocity deficit (left) and radial velocity (right) as a function of r/r_{ci} in the plane $x = x_{mid}$ with $\beta = 0.0446$.

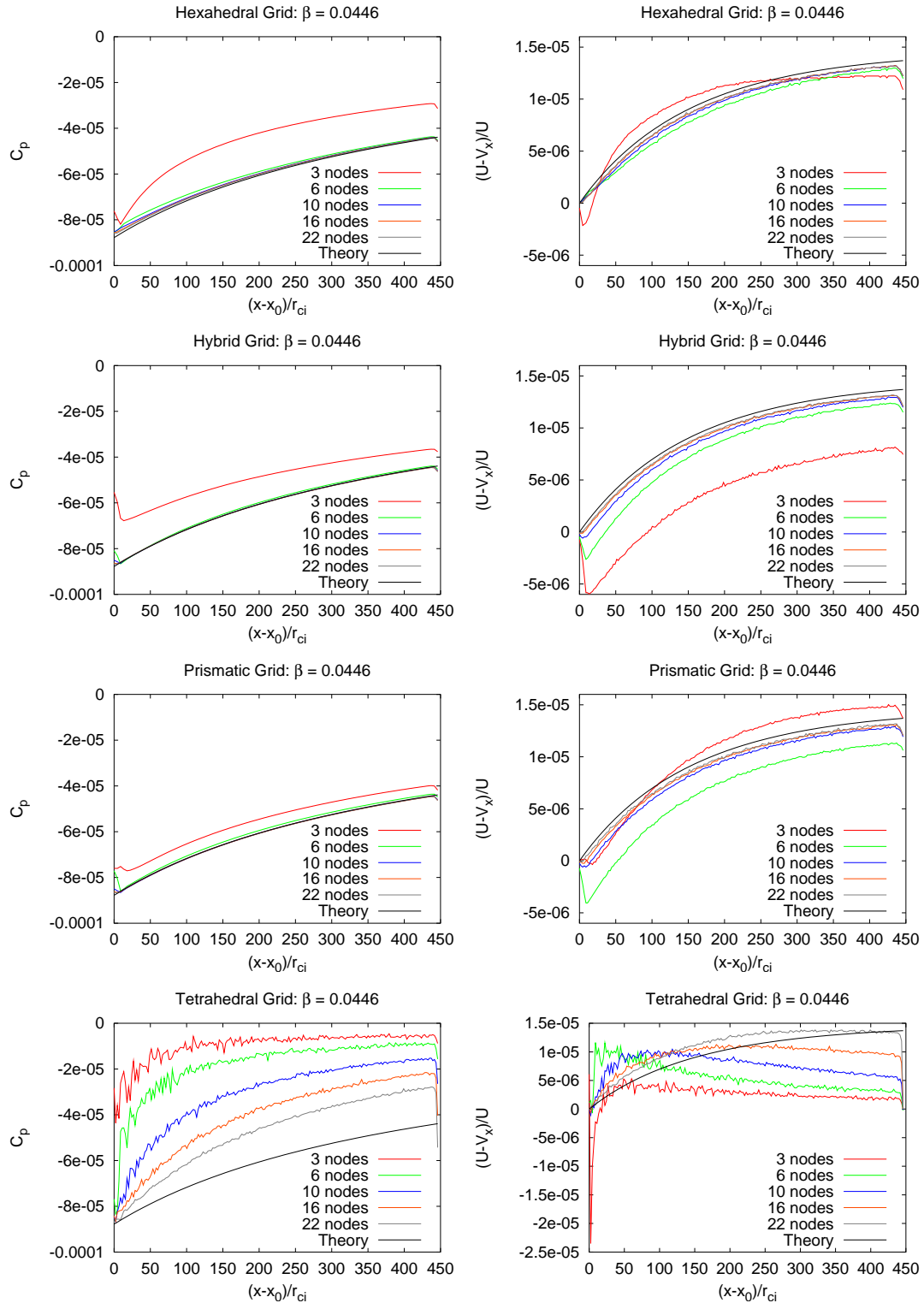


Figure A.3: Laminar vortex: the pressure coefficient (left) and axial velocity deficit (right) as a function of $(x - x_0)/r_{ci}$ on the centreline with $\beta = 0.0446$.

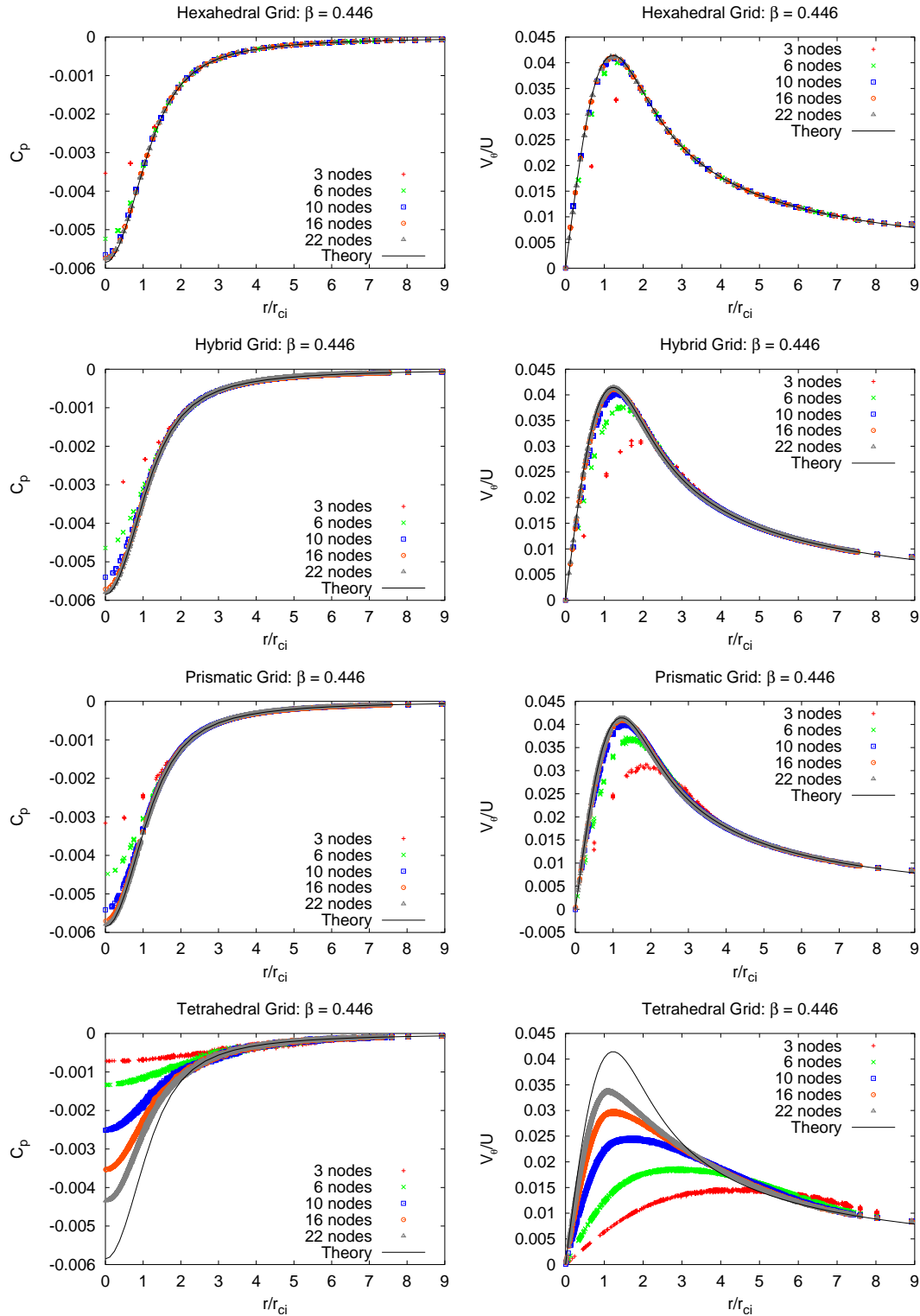


Figure A.4: Laminar vortex: the pressure coefficient (left) and circumferential velocity (right) as a function of r/r_{ci} in the plane $x = x_{mid}$ with $\beta = 0.446$.

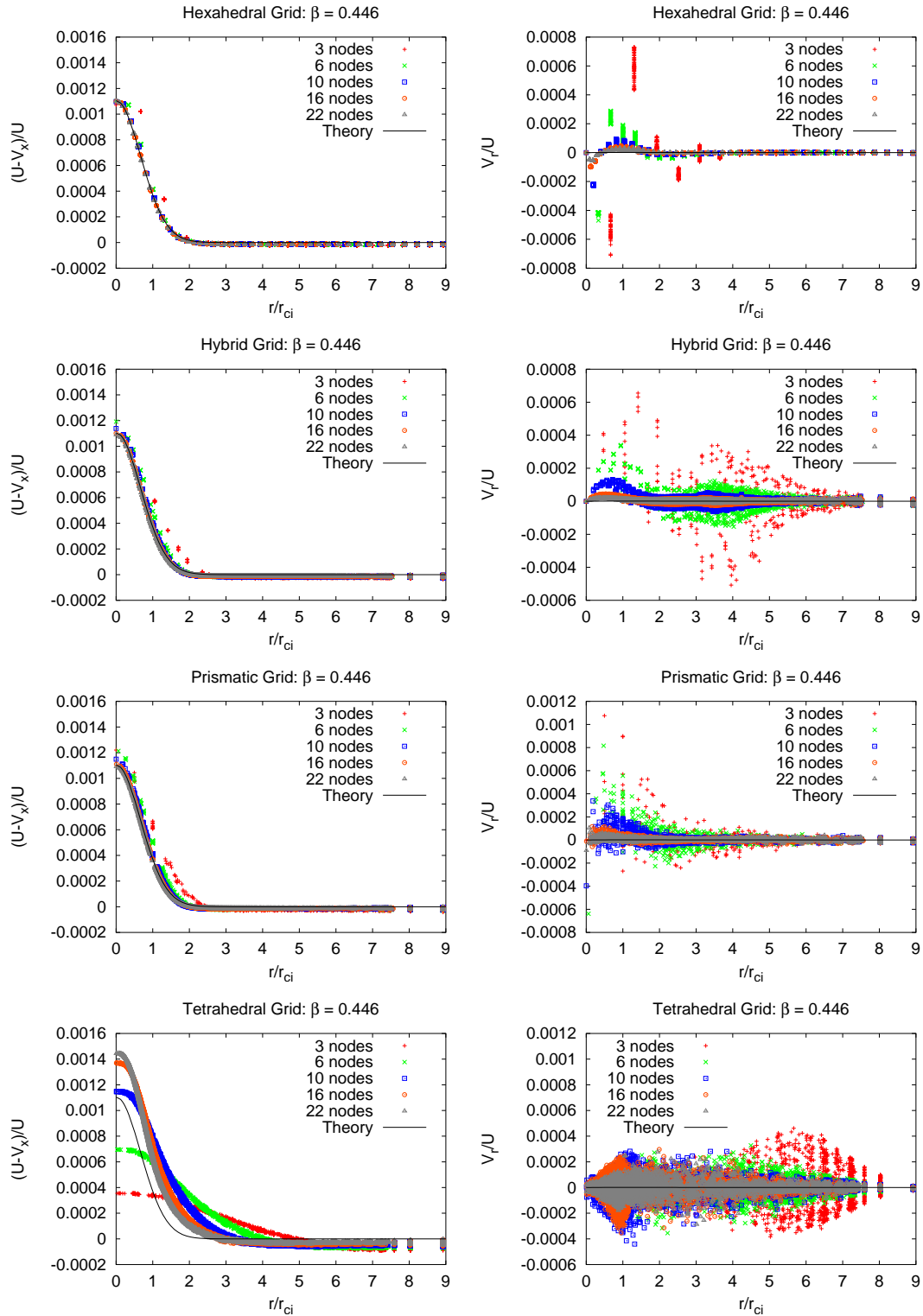


Figure A.5: Laminar vortex: the axial velocity deficit (left) and radial velocity (right) as a function of r/r_{ci} in the plane $x = x_{mid}$ with $\beta = 0.446$.

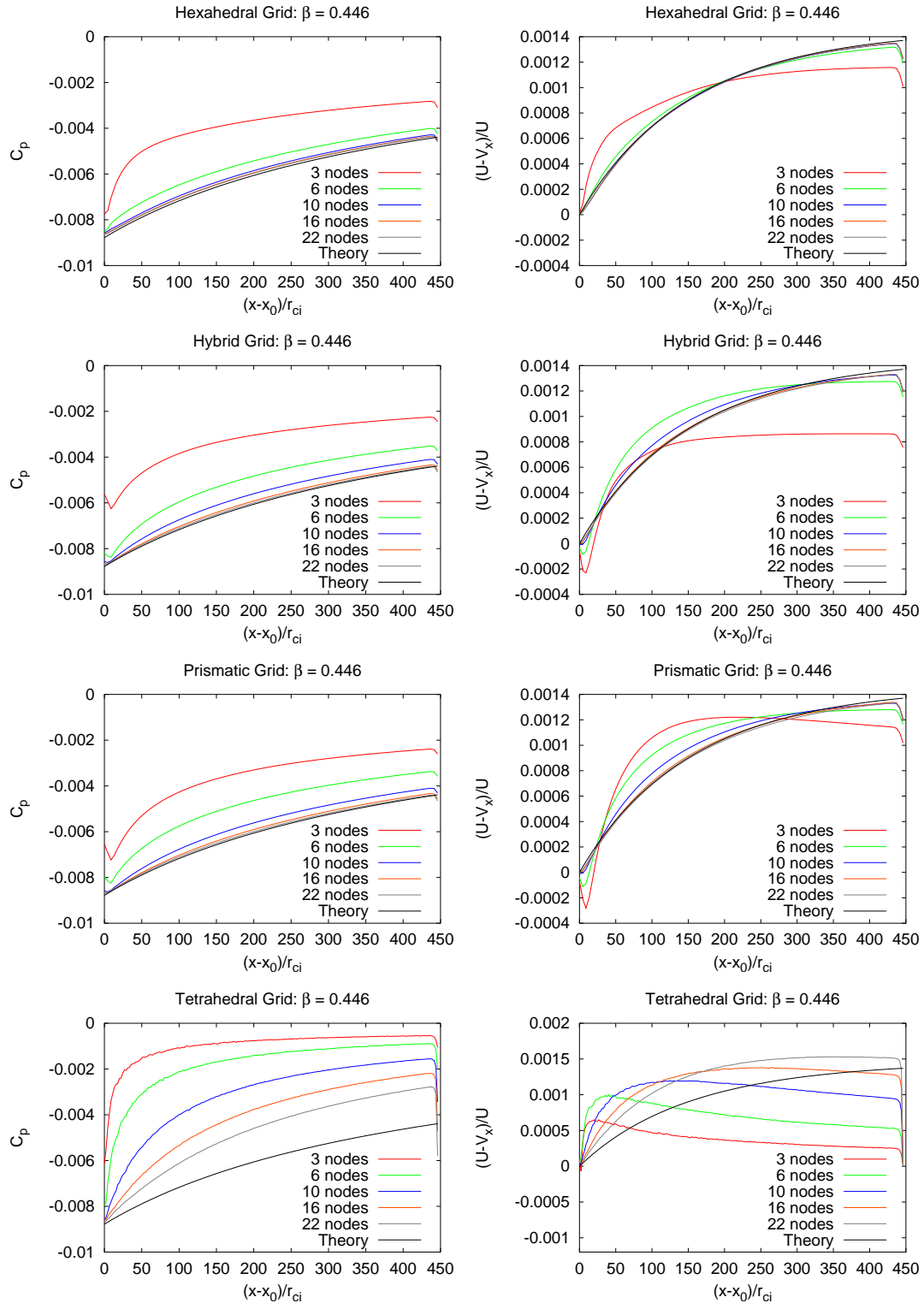


Figure A.6: Laminar vortex: the pressure coefficient (left) and axial velocity deficit (right) as a function of $(x - x_0)/r_{ci}$ on the centreline: $\beta = 0.446$.

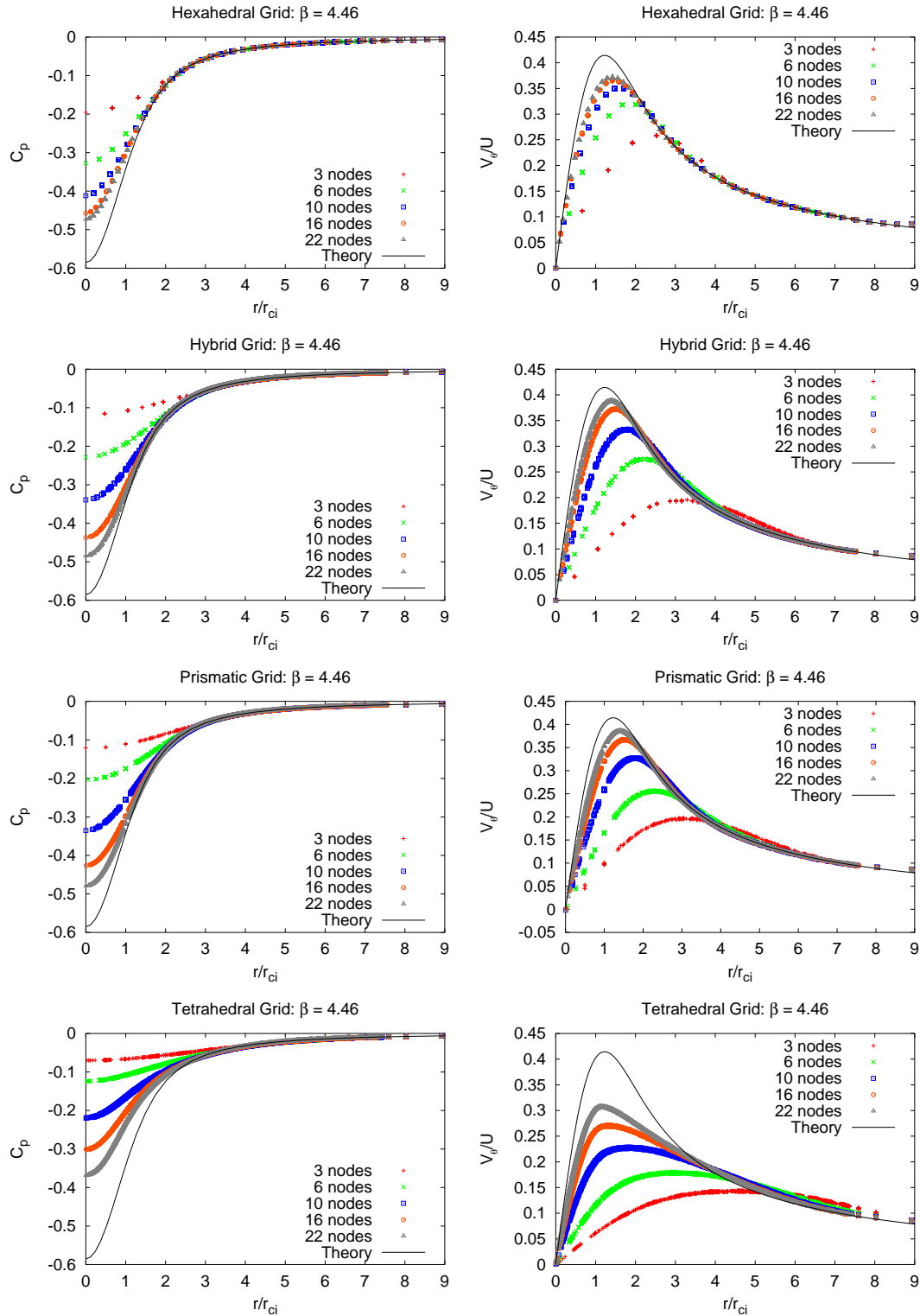


Figure A.7: Laminar vortex: the pressure coefficient (left) and circumferential velocity v_θ/U (right) as a function of r/r_{ci} in the plane $x = x_{mid}$ with $\beta = 4.461$.

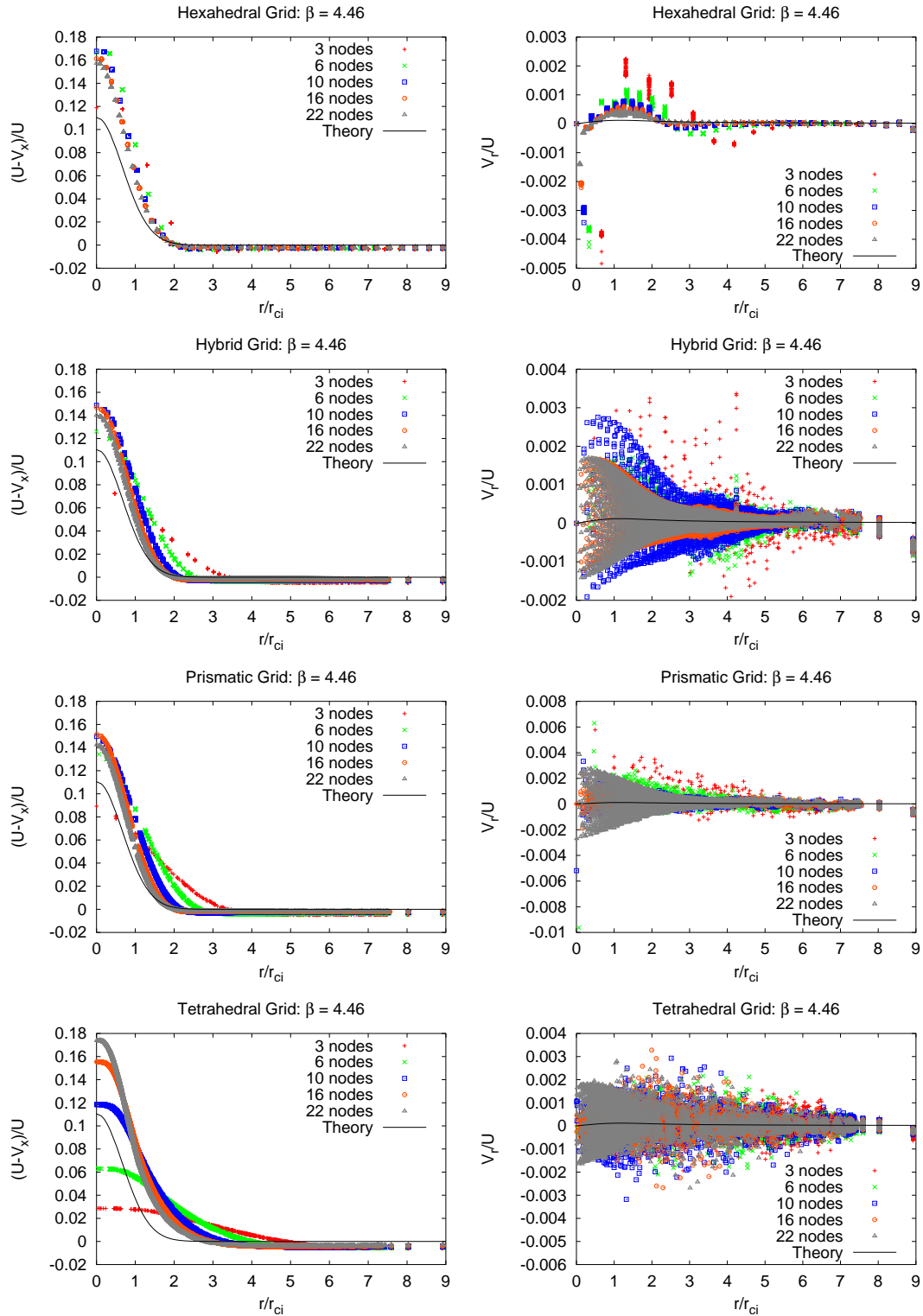


Figure A.8: Laminar vortex: the axial velocity deficit (left) and radial velocity (right) as a function of r/r_{ci} in the plane $x = x_{mid}$ with $\beta = 4.461$.

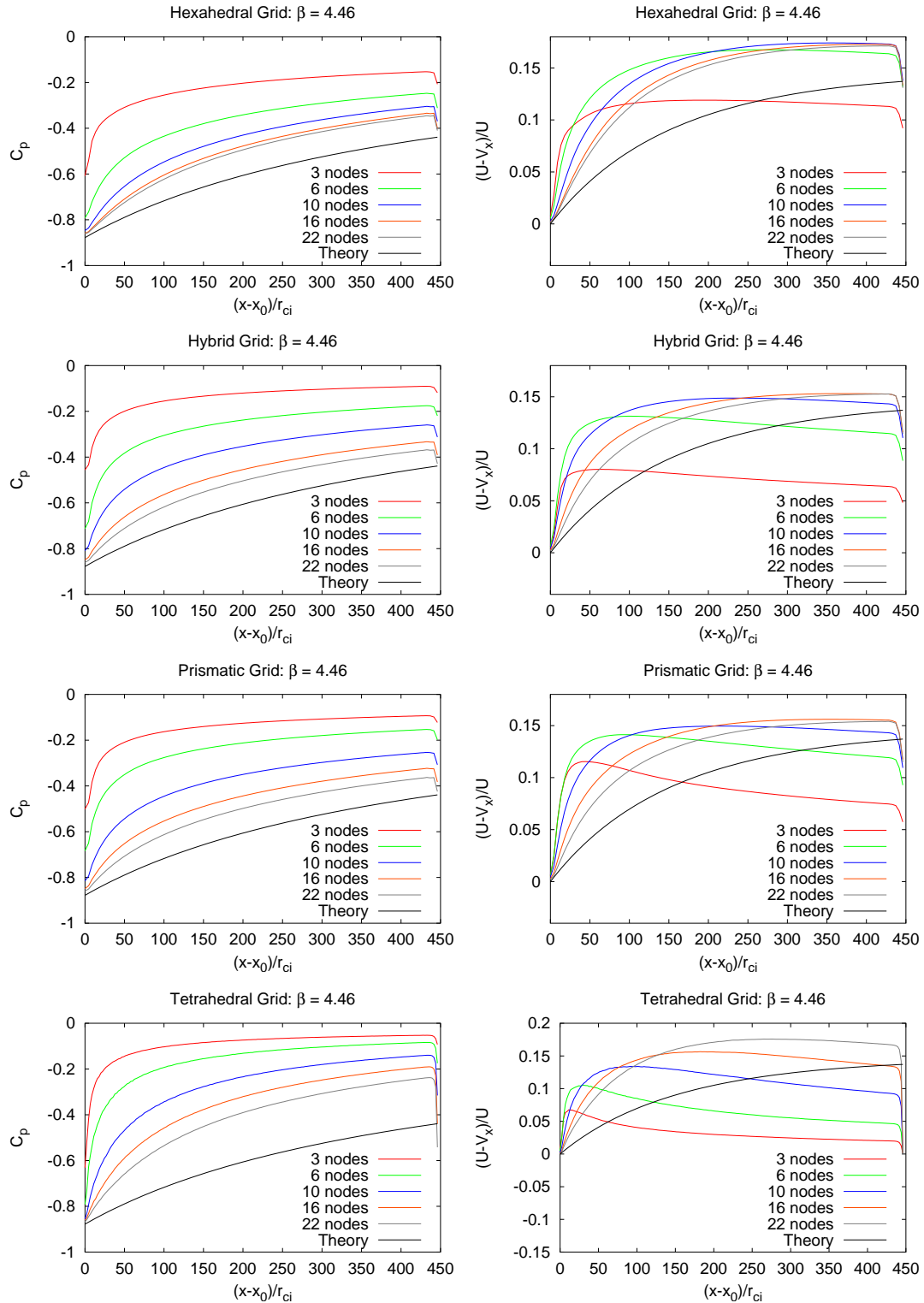


Figure A.9: Laminar vortex: the pressure coefficient (left) and axial velocity deficit (right) as a function of $(x - x_0)/r_{ci}$ on the centreline: $\beta = 4.461$.

Annex B: Results of the turbulent computations

The figures on the following pages show the results of the turbulent computations for each type of grid. For each grid and for each value of the circulation parameter β , six plots are presented:

1. pressure coefficient as a function of r/r_{ci} in the plane $x = x_{mid}$;
2. the circumferential velocity, v_θ/U , as a function of r/r_{ci} in the plane $x = x_{mid}$;
3. the axial velocity deficit, $(U - v_x)/U$, as a function of r/r_{ci} in the plane $x = x_{mid}$;
4. the non-dimensional turbulent viscosity, ν_t/Ur_{ci} , as a function of r/r_{ci} in the plane $x = x_{mid}$ metres;
5. the pressure coefficient along the centreline as a function of the distance from the initial plane measured in core radii (i.e. $(x - x_0)/r_{ci}$); and
6. the non-dimensional turbulent viscosity, ν_t/Ur_{ci} , along the centreline, as a function of the distance from the initial plane measured in core radii.

Each plot shows the results for six runs with varying numbers of nodes across the vortex core.

For easy comparison between the different grids, the results for each of the three grid types are shown on the same page.

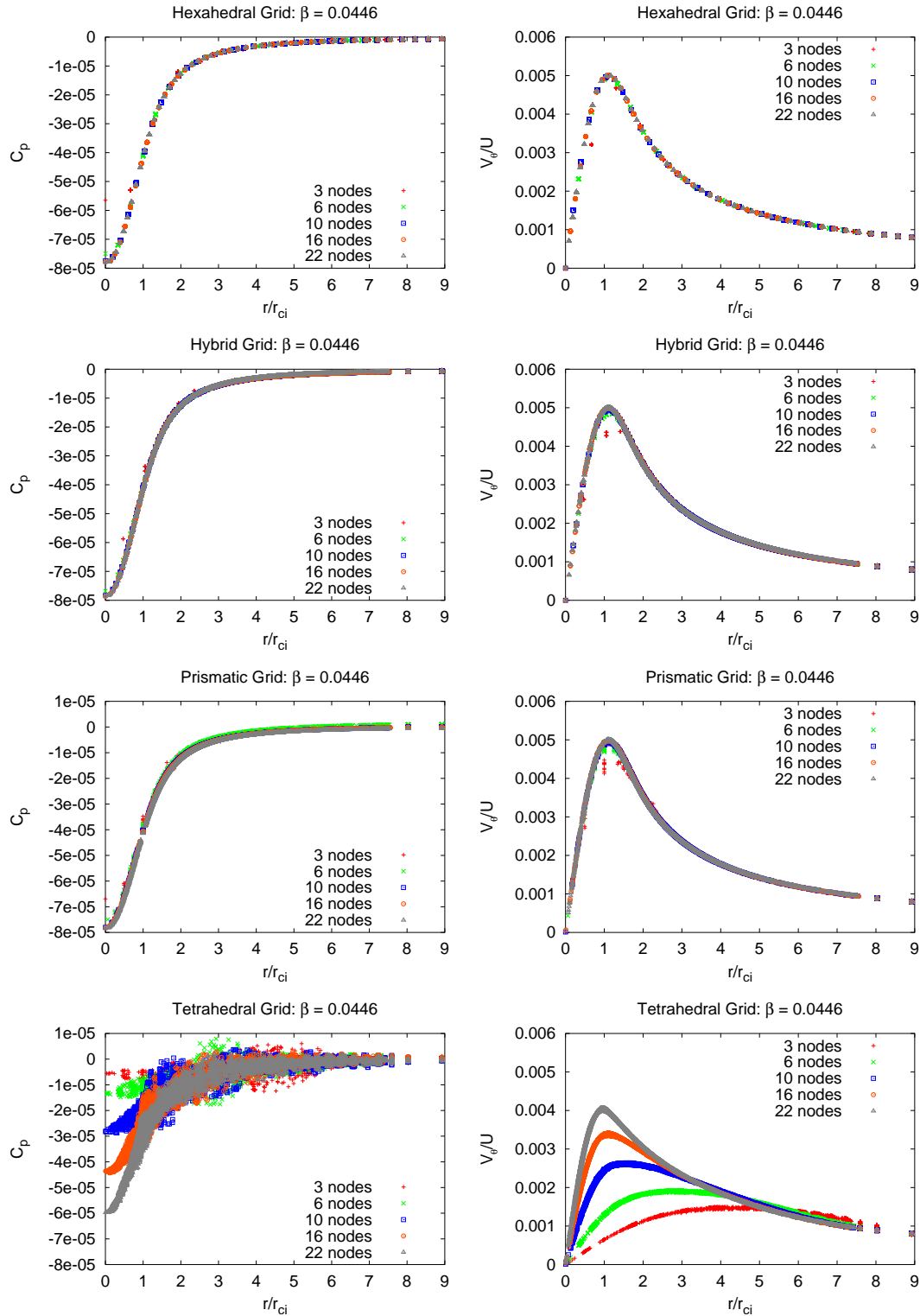


Figure B.1: Turbulent vortex: the pressure coefficient (left) and circumferential velocity (right) as a function of r/r_{ci} in the plane $x = x_{mid}$ with $\beta = 0.0446$.

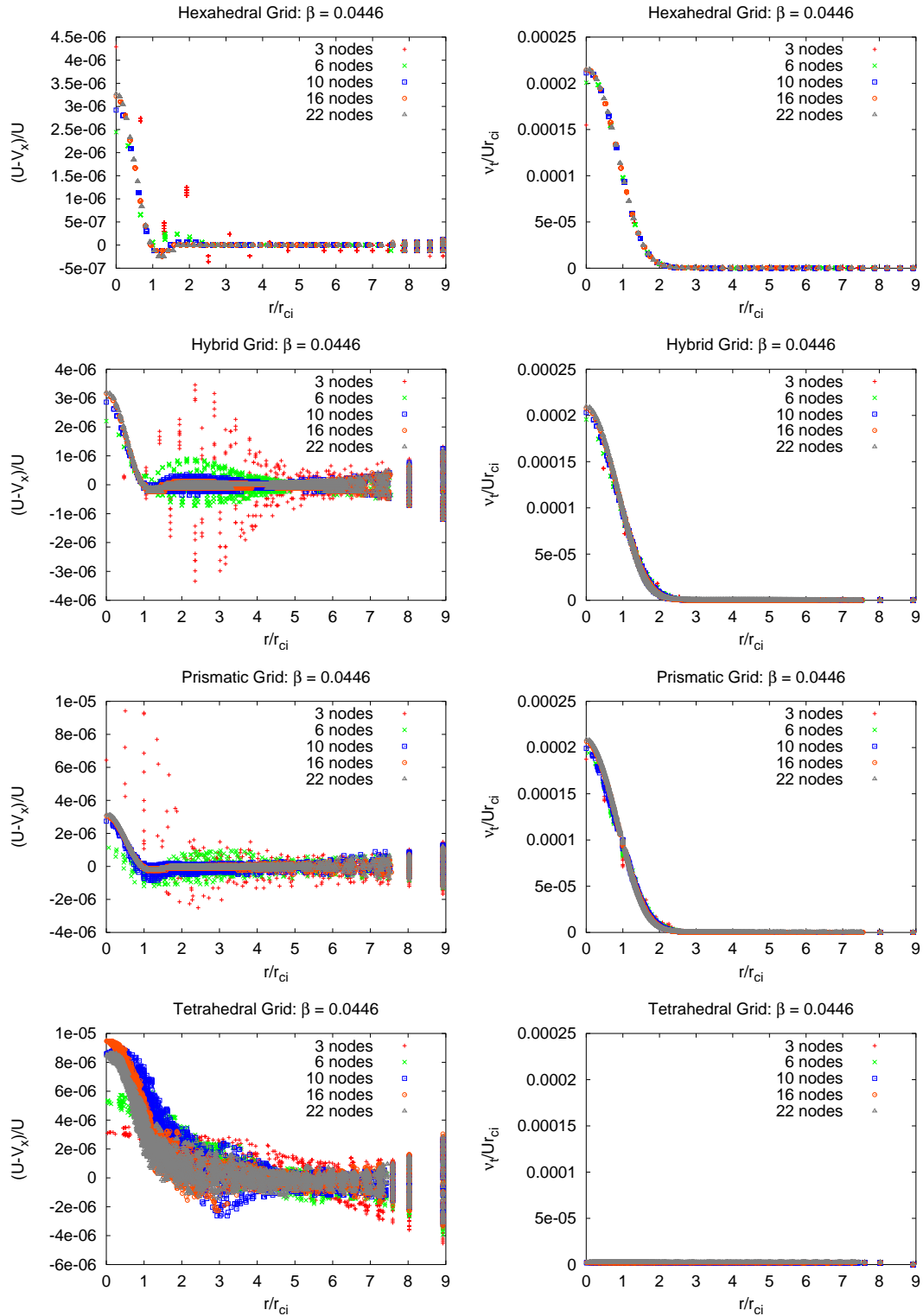


Figure B.2: Turbulent vortex: the axial velocity deficit (left) and the turbulent viscosity (right) as a function of r/r_{ci} in the plane $x = x_{mid}$ with $\beta = 0.0446$.

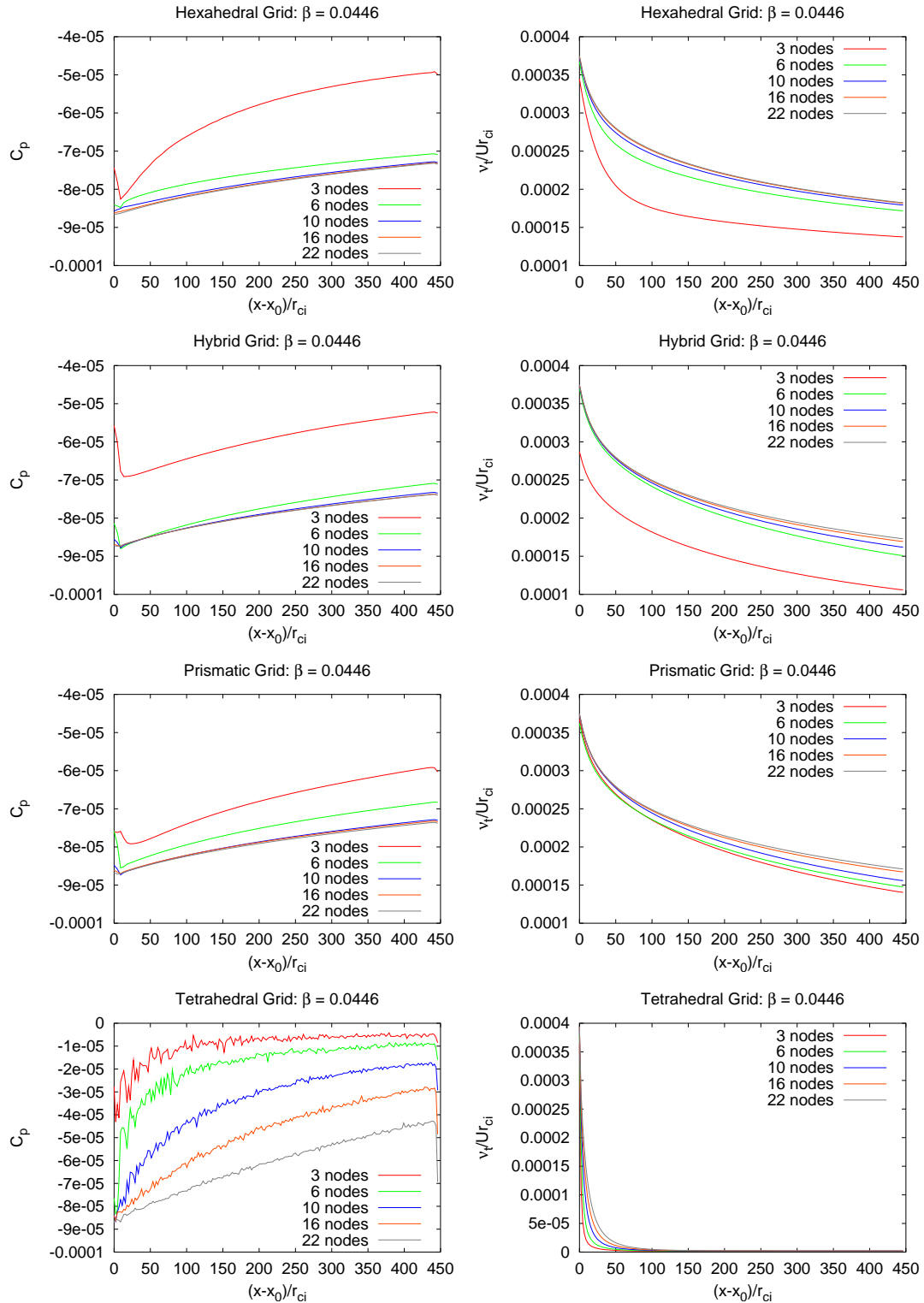


Figure B.3: Turbulent vortex: the pressure coefficient (left) and the turbulent viscosity (right) as a function of $(x - x_0)/r_{ci}$ on the centreline: $\beta = 0.0446$.

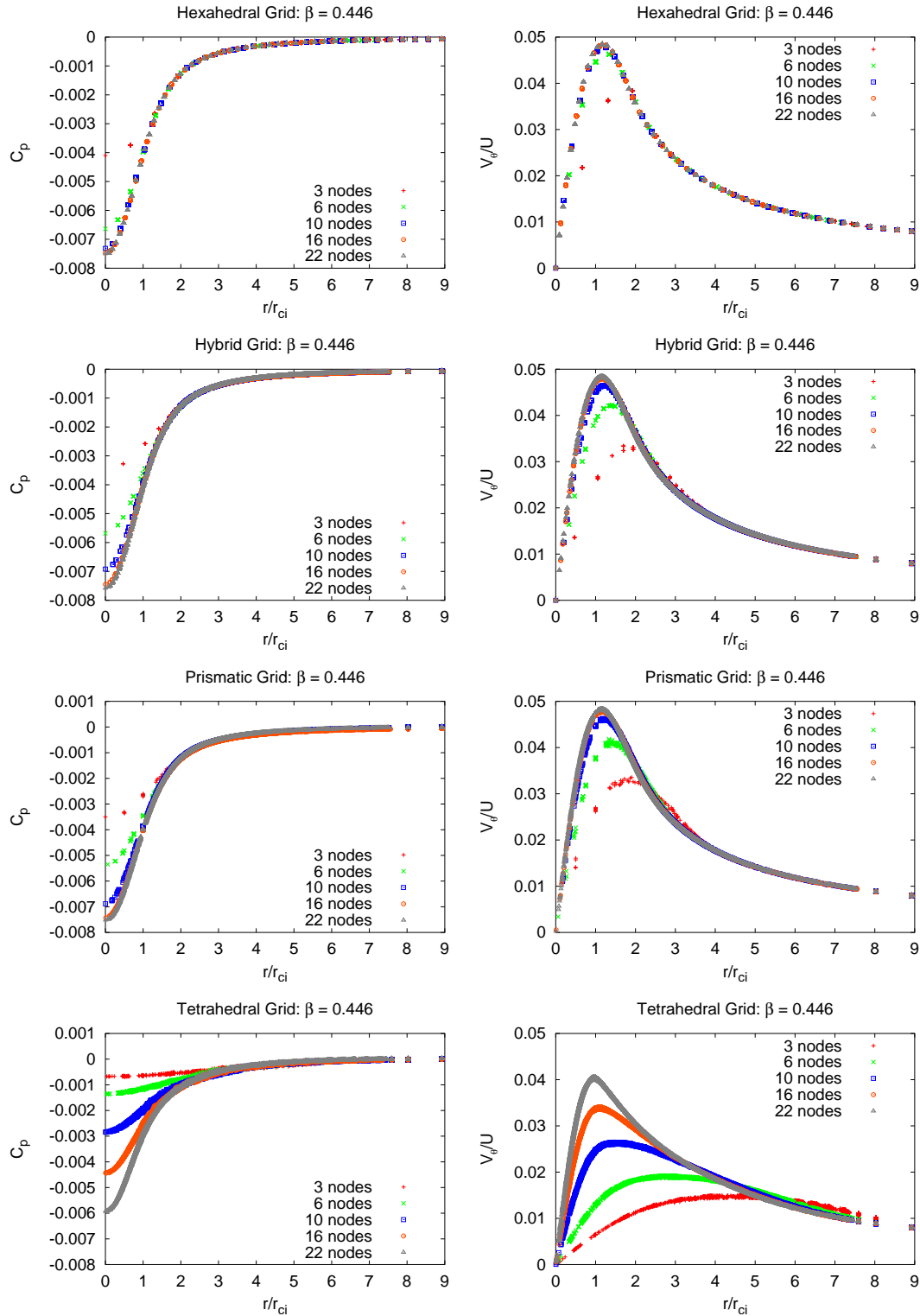


Figure B.4: Turbulent vortex: the pressure coefficient (left) and circumferential velocity v_θ/U (right) as a function of r/r_{ci} in the plane $x = x_{mid}$ with $\beta = 0.446$.

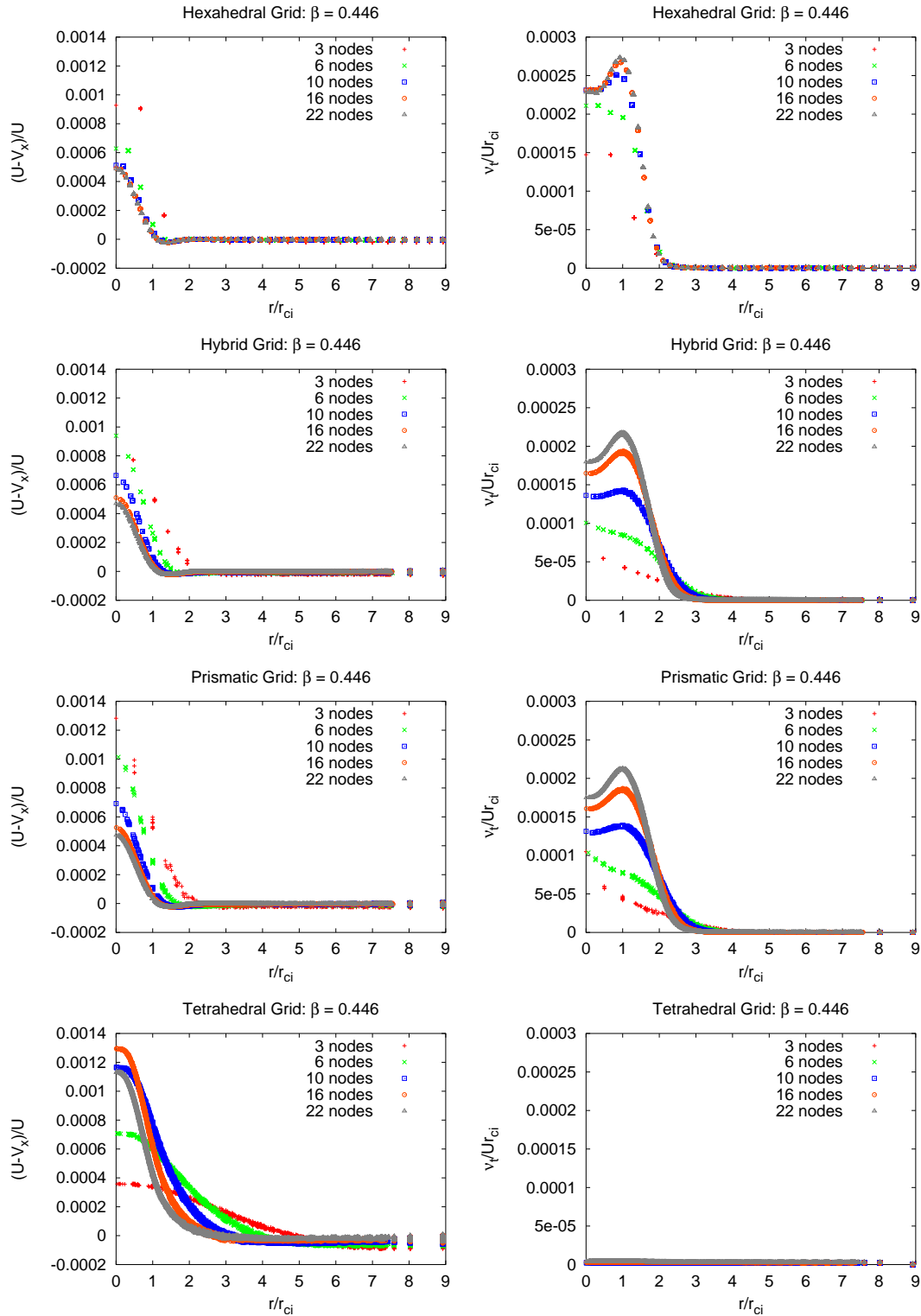


Figure B.5: Turbulent vortex: the axial velocity deficit (left) and the turbulent viscosity (right) as a function of r/r_{ci} in the plane $x = x_{mid}$ with $\beta = 0.446$.

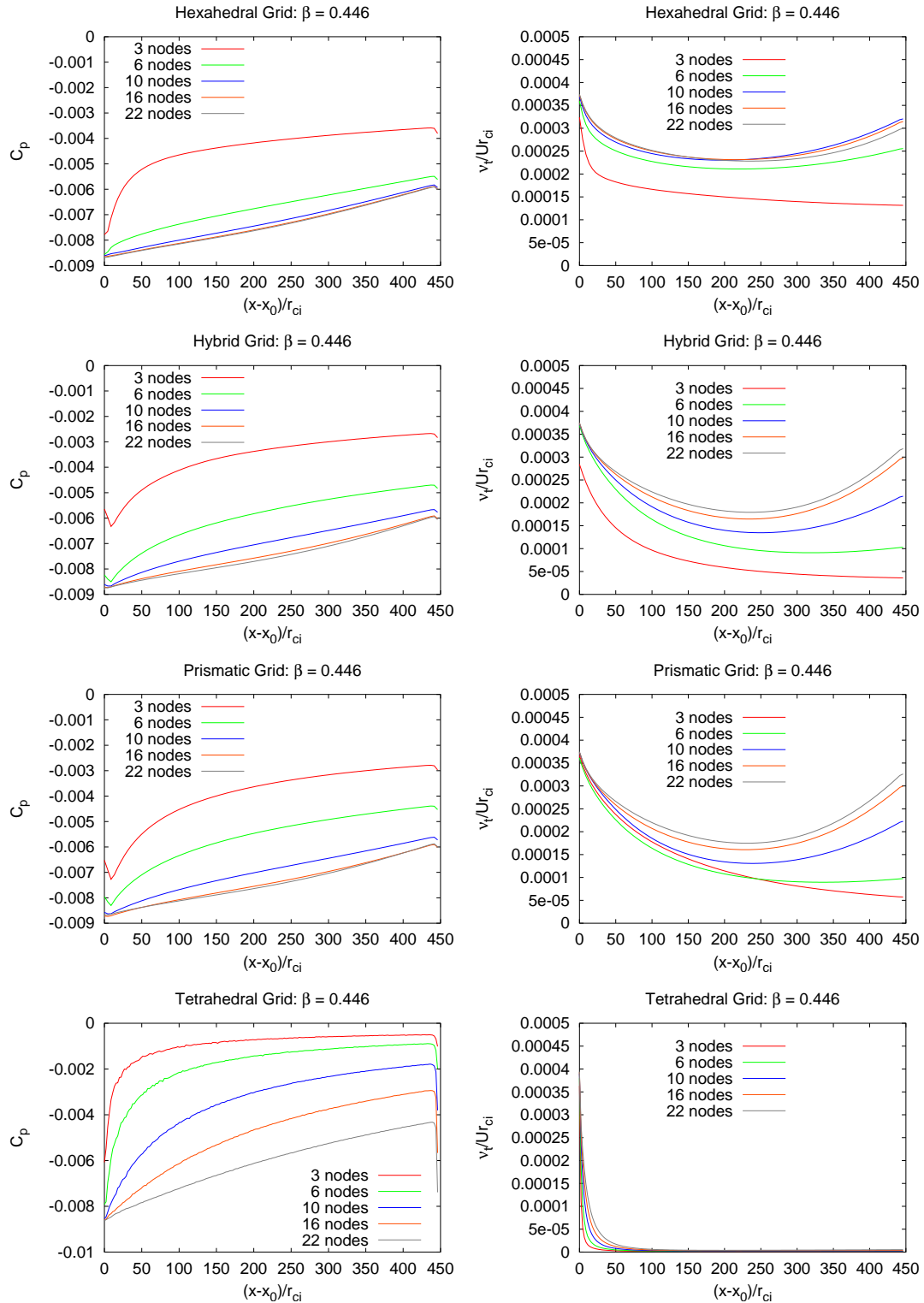


Figure B.6: Turbulent vortex: the pressure coefficient (left) and the turbulent viscosity (right) as a function of $(x - x_0)/r_{ci}$ on the centreline: $\beta = 0.446$.

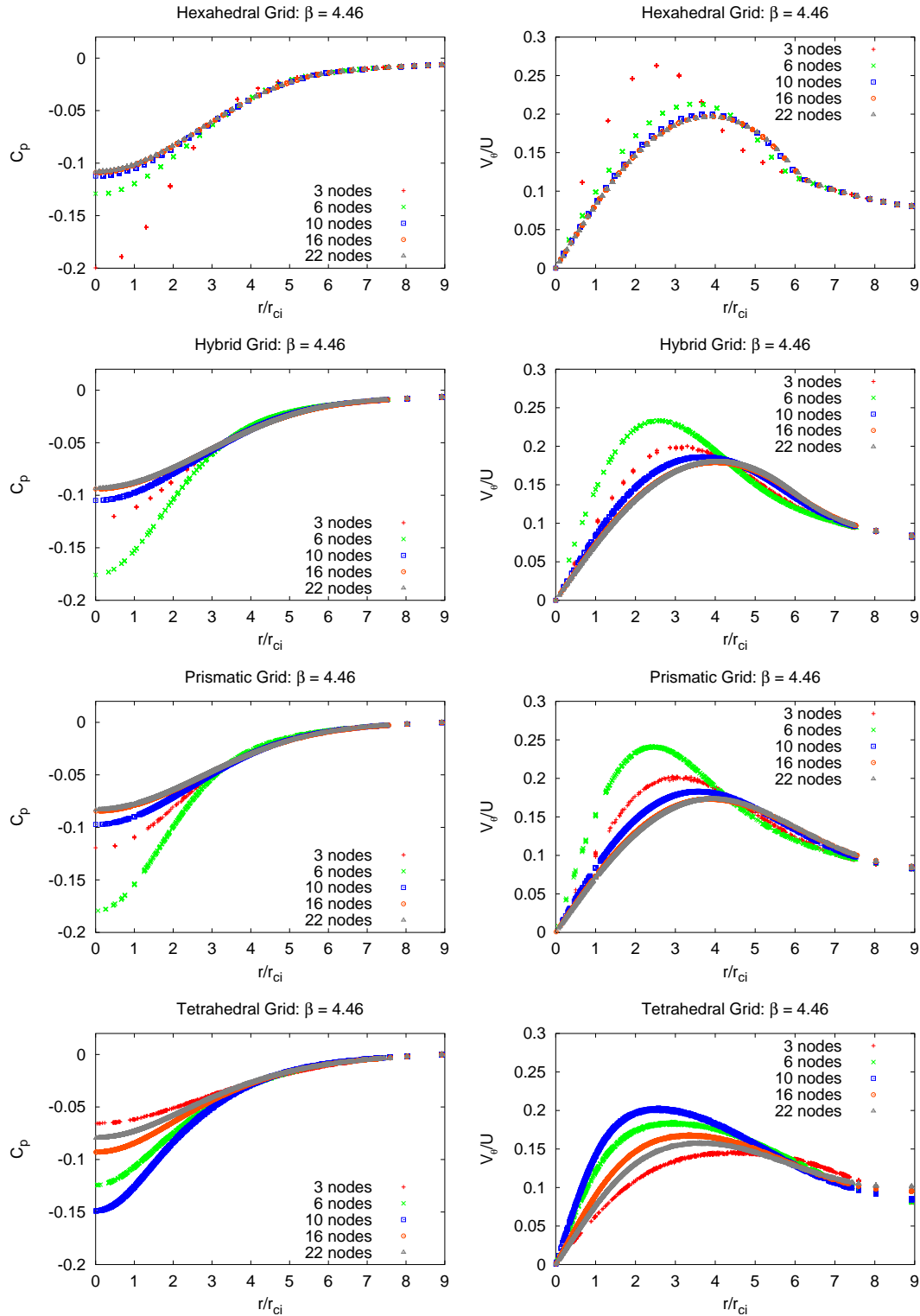


Figure B.7: Turbulent vortex: the pressure coefficient (left) and circumferential velocity (right) as a function of r/r_{ci} in the plane $x = x_{mid}$ with $\beta = 4.461$.

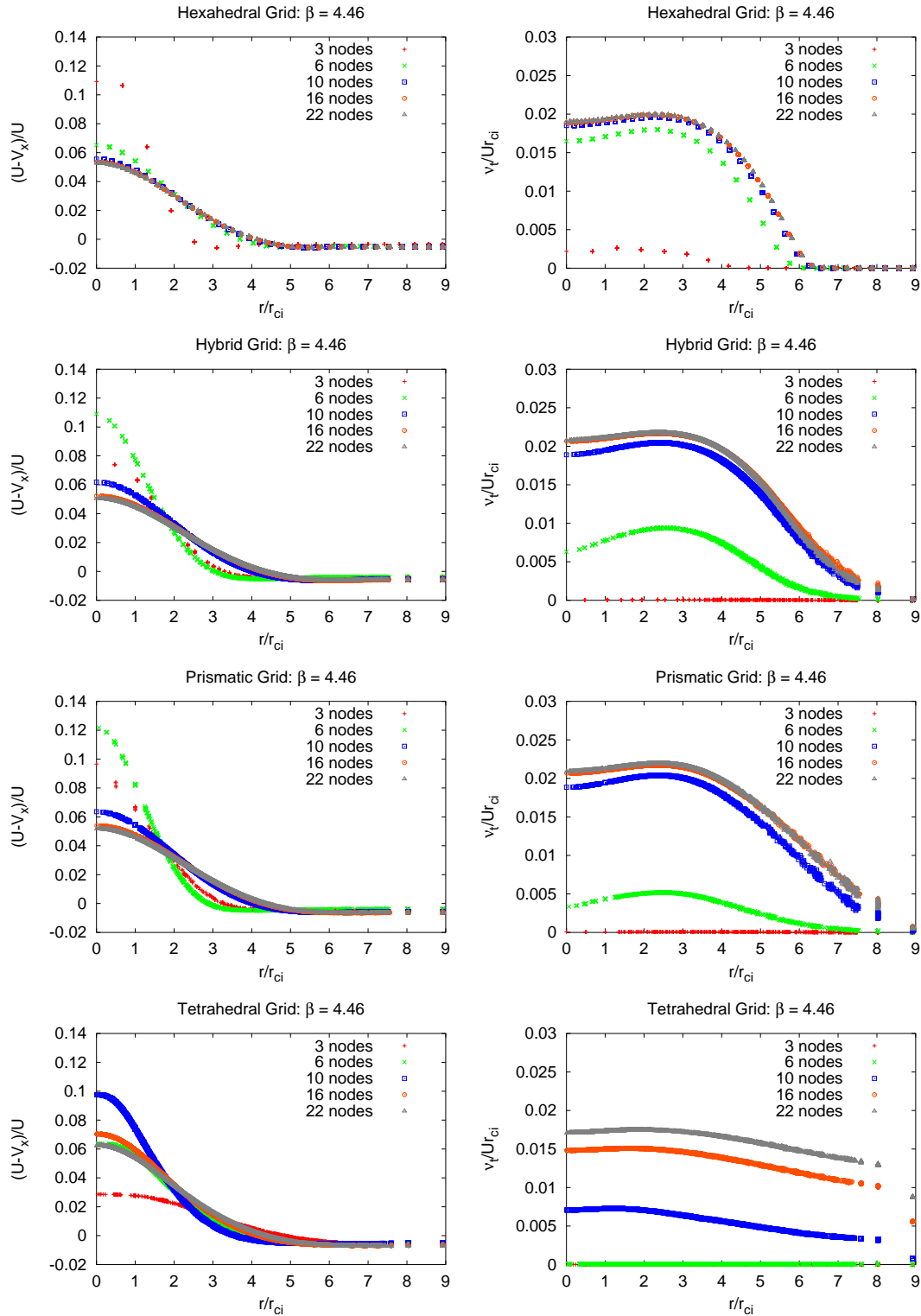


Figure B.8: Turbulent vortex: the axial velocity deficit (left) and the turbulent viscosity (right) as a function of r/r_{ci} in the plane $x = x_{mid}$ with $\beta = 4.461$.

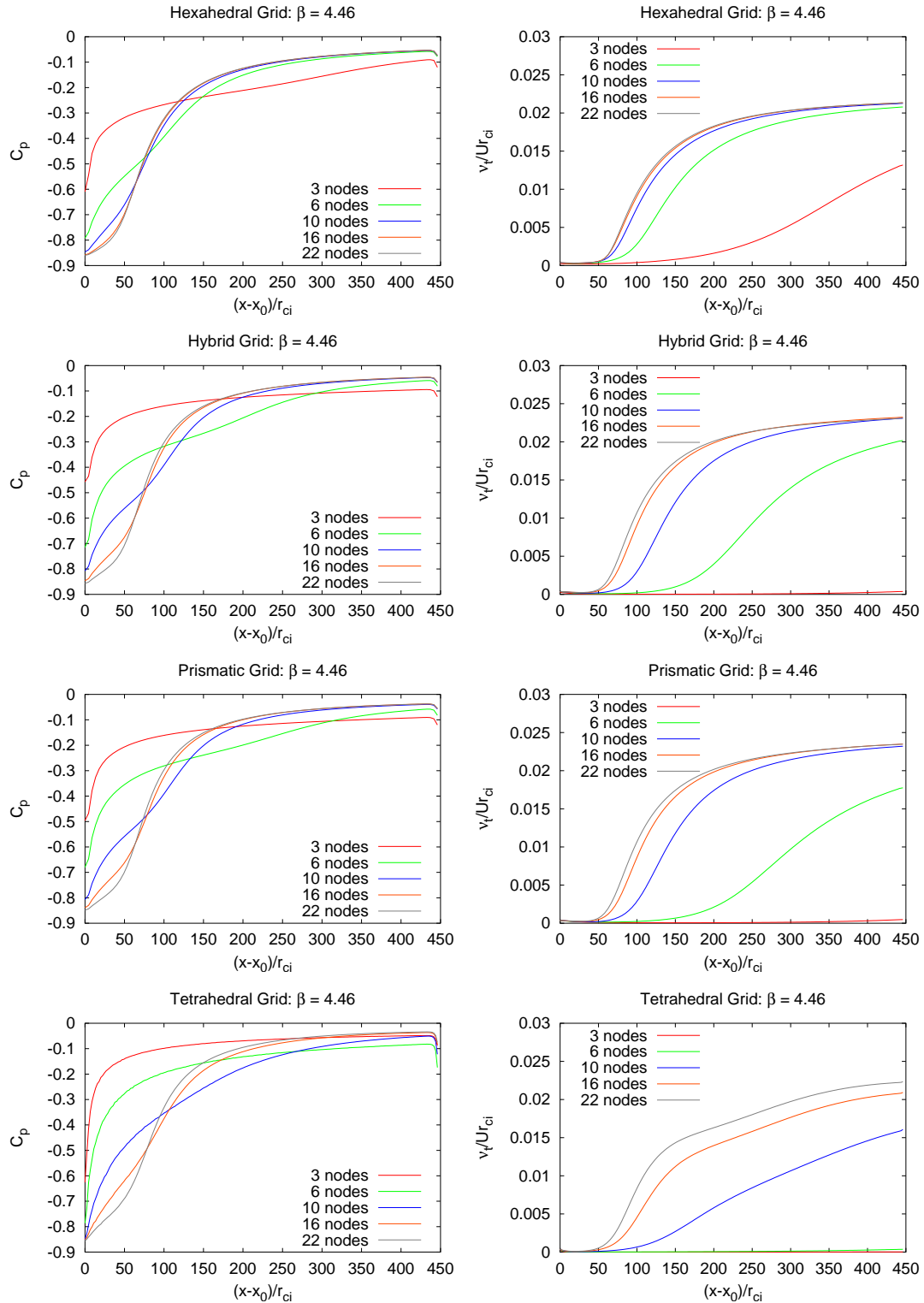


Figure B.9: Turbulent vortex: the pressure coefficient (left) and the turbulent viscosity (right) as a function of $(x - x_0)/r_{ci}$ on the centerline: $\beta = 4.461$.

Annex C: Perturbation expansion of the vortex solution

To get a firm grasp on the size of the errors in the approximate vortex solution, we express this solution as a perturbation expansion in a small parameter ϵ . We assume that U is of order 1 and v_θ is of order ϵ . From Eq. (6), that implies that

$$\frac{v_{\theta \max}}{U} = 0.114 \frac{C}{U r_c} = 0.114 \beta \quad (\text{C.1})$$

is of order ϵ . Therefore the approximation is valid if $\beta \ll 9$. If we let r_c be of order 1 (this simply sets a length scale for the flow), then C must be of order ϵ .

Furthermore, to model the dominance of convection over diffusion, we assume that derivatives with respect to x are of order ϵ : i.e. r_c/x is of order ϵ . Since $r_c \approx 2.24\sqrt{\nu x/U}$, this implies that $5\nu/U r_c \ll 1$ and ν is of order ϵ .

Let

$$C = \epsilon C^*; \quad \nu = \epsilon \nu^*; \quad x = x^*/\epsilon \quad (\text{C.2})$$

and assume a solution of the form:

$$v_x(x^*, r) = \sum_i \epsilon^i v_x^{(i)}(x^*, r) \quad (\text{C.3})$$

$$v_r(x^*, r) = \sum_i \epsilon^i v_r^{(i)}(x^*, r) \quad (\text{C.4})$$

$$v_\theta(x^*, r) = \sum_i \epsilon^i v_\theta^{(i)}(x^*, r) \quad (\text{C.5})$$

$$p(x^*, r) = \sum_i \epsilon^i p^{(i)}(x^*, r) \quad (\text{C.6})$$

To conform with the approximate solution we have

$$v_x^{(0)}(x^*, r) = U \quad (\text{C.7})$$

$$v_r^{(0)}(x^*, r) = v_r^{(1)}(x^*, r) = 0 \quad (\text{C.8})$$

$$v_\theta^{(0)}(x^*, r) = 0 \quad (\text{C.9})$$

$$v_\theta^{(1)} = \frac{C^*}{2\pi r} \left(1 - e^{-\frac{U r^2}{4\nu^* x^*}}\right) \quad (\text{C.10})$$

$$p^{(0)}(x^*, r) = p^{(1)}(x^*, r) = 0 \quad (\text{C.11})$$

$$p^{(2)}(x^*, r) = -\frac{\rho C^{*2}}{4\pi^2} \int_r^\infty \frac{1}{z^3} \left(1 - e^{-\frac{U z^2}{4\nu^* x^*}}\right)^2 dz \quad (\text{C.12})$$

From here on we will drop the asterisks on the perturbed variables. Since we will no longer use the original variables, this should cause no confusion.

The Navier-Stokes equations for steady axisymmetric flow in cylindrical coordinates can be written:

$$\epsilon \frac{\partial v_x}{\partial x} + \frac{1}{r} \frac{\partial(rv_r)}{\partial r} = 0 \quad (\text{C.13})$$

$$\epsilon v_x \frac{\partial v_x}{\partial x} + v_r \frac{\partial v_x}{\partial r} = -\frac{\epsilon}{\rho} \frac{\partial p}{\partial x} + \epsilon \nu \left(\epsilon^2 \frac{\partial^2 v_x}{\partial x^2} + \frac{1}{r} \frac{\partial}{\partial r} \left(r \frac{\partial v_x}{\partial r} \right) \right) \quad (\text{C.14})$$

$$\epsilon v_x \frac{\partial v_r}{\partial x} + v_r \frac{\partial v_r}{\partial r} - \frac{v_\theta^2}{r} = -\frac{1}{\rho} \frac{\partial p}{\partial r} + \epsilon \nu \left(\epsilon^2 \frac{\partial^2 v_r}{\partial x^2} + \frac{1}{r} \frac{\partial}{\partial r} \left(r \frac{\partial v_r}{\partial r} \right) - \frac{v_r}{r^2} \right) \quad (\text{C.15})$$

$$\epsilon v_x \frac{\partial v_\theta}{\partial x} + v_r \frac{\partial v_\theta}{\partial r} + \frac{v_r v_\theta}{r} = \epsilon \nu \left(\epsilon^2 \frac{\partial^2 v_\theta}{\partial x^2} + \frac{1}{r} \frac{\partial}{\partial r} \left(r \frac{\partial v_\theta}{\partial r} \right) - \frac{v_\theta}{r^2} \right) \quad (\text{C.16})$$

Substituting Eqs. (C.7)–(C.12) into Eqs. (C.13)–(C.16) and retaining only the lowest order of ϵ in each equation we get:

$$\frac{\partial v_x^{(1)}}{\partial x} + \frac{1}{r} \frac{\partial(rv_r^{(2)})}{\partial r} = 0 \quad (\text{C.17})$$

$$U \frac{\partial v_x^{(1)}}{\partial x} = \frac{\nu}{r} \frac{\partial}{\partial r} \left(r \frac{\partial v_x^{(1)}}{\partial r} \right) \quad (\text{C.18})$$

$$\frac{(v_\theta^{(1)})^2}{r} = \frac{1}{\rho} \frac{\partial p^{(2)}}{\partial r} \quad (\text{C.19})$$

$$U \frac{\partial v_\theta^{(1)}}{\partial x} = \nu \left(\frac{1}{r} \frac{\partial}{\partial r} \left(r \frac{\partial v_\theta^{(1)}}{\partial r} \right) - \frac{v_\theta^{(1)}}{r^2} \right) \quad (\text{C.20})$$

Eqs. (C.19) and (C.20) have solutions given by Eqs. (C.10) and (C.12). Eq. (C.18) can be solved for $v_x^{(1)}$; the solution with $v_x^{(1)}(x_0, r) = 0$ is simply $v_x^{(1)}(x, r) = 0$. Eq. (C.17) then implies that $v_r^{(2)}(x, r) = 0$.

Proceeding to the next level of expansion we get:

$$\frac{\partial v_x^{(2)}}{\partial x} + \frac{1}{r} \frac{\partial(rv_r^{(3)})}{\partial r} = 0 \quad (\text{C.21})$$

$$U \frac{\partial v_x^{(2)}}{\partial x} = -\frac{1}{\rho} \frac{\partial p^{(2)}}{\partial x} + \frac{\nu}{r} \frac{\partial}{\partial r} \left(r \frac{\partial v_x^{(2)}}{\partial r} \right) \quad (\text{C.22})$$

$$\frac{2v_\theta^{(1)}v_\theta^{(2)}}{r} = \frac{1}{\rho} \frac{\partial p^{(3)}}{\partial r} \quad (\text{C.23})$$

$$U \frac{\partial v_\theta^{(2)}}{\partial x} = \nu \left(\frac{1}{r} \frac{\partial}{\partial r} \left(r \frac{\partial v_\theta^{(2)}}{\partial r} \right) - \frac{v_\theta^{(2)}}{r^2} \right) \quad (\text{C.24})$$

Eq. (C.24) implies that $v_\theta^{(2)} = 0$ to satisfy the initial condition that $v_\theta^{(2)}(x_0, r) = 0$. Then Eq. (C.23) implies that $p^{(3)} = 0$.

Let

$$z = \frac{r^2 U}{4\nu x} \quad (\text{C.25})$$

Then

$$p^{(2)} = -\frac{\rho C^2}{4\pi^2} \int_r^\infty \frac{1}{z^3} \left(1 - e^{-\frac{Uz^2}{4\nu x}}\right)^2 dz = -\frac{\rho C^2 U}{32\pi^2 \nu x} f(z) \quad (\text{C.26})$$

where

$$f(z) = \int_z^\infty \left(\frac{1 - e^{-y}}{y}\right)^2 dy \quad (\text{C.27})$$

We look for a full solution to $v_x^{(2)}$ of the form

$$v_x^{(2)}(x, r) = \frac{C^2}{32\pi^2 \nu} \sum_{n=1}^\infty \frac{(x - x_0)^n}{x^{n+1}} g_n(z) \quad (\text{C.28})$$

Substituting into Eq. (C.22) we find that

$$\sum_{n=0}^\infty \frac{(x - x_0)^n}{x^n} \left((n+1)g_{n+1}(z) - (n+1)g_n(z) - (1+z)g'_n(z) - zg''_n(z) \right) = -f(z) - zf'(z) \quad (\text{C.29})$$

provided that we define $g_0(z) = 0$. Therefore,

$$g_0(z) = 0 \quad (\text{C.30})$$

$$g_1(z) = -f(z) - zf'(z) \quad (\text{C.31})$$

$$g_{n+1}(z) = g_n(z) + \frac{(1+z)g'_n(z) + zg''_n(z)}{n+1} \quad (\text{C.32})$$

Let $h_n(z) = (g_n(z) - g_1(z))e^{2z}$. Then

$$\begin{aligned} v_x^{(2)}(x, r) &= \frac{C^2}{32\pi^2 \nu} \sum_{n=1}^\infty \frac{(x - x_0)^n}{x^{n+1}} (g_1(z) + h_n(z)e^{-2z}) \\ &= \frac{C^2}{32\pi^2 \nu} \left[\frac{g_1(z)(x - x_0)}{xx_0} + \sum_{n=2}^\infty \frac{(x - x_0)^n}{x^{n+1}} h_n(z)e^{-2z} \right] \\ &= -\frac{C^2(x - x_0)}{32\pi^2 \nu x x_0} \left[f(z) - \frac{(1 - e^{-z})^2}{z} - \frac{x_0 e^{-2z}}{x} \sum_{n=1}^\infty \left(\frac{x - x_0}{x}\right)^n h_{n+1}(z) \right] \end{aligned} \quad (\text{C.33})$$

The functions $h_n(z)$ are polynomials in z which can be determined from a recursion obtained from the recursion relation for $g_n(z)$:

$$h_1(z) = 0 \quad (\text{C.34})$$

$$h_{n+1}(z) = h_n(z) + \frac{2(z-1)h_n(z) + (1-3z)h'_n(z) + zh''_n(z) + 2}{n+1} \quad (\text{C.35})$$

The first few $h_n(z)$ are:

$$h_1(z) = 0 \quad (\text{C.36})$$

$$h_2(z) = 1 \quad (\text{C.37})$$

$$h_3(z) = 1 + \frac{2z}{3} \quad (\text{C.38})$$

$$h_4(z) = \frac{7}{6} + \frac{z}{3} + \frac{z^2}{3} \quad (\text{C.39})$$

$$h_5(z) = \frac{7}{6} + \frac{11z}{15} - \frac{z^2}{15} + \frac{2z^3}{15} \quad (\text{C.40})$$

$$h_6(z) = \frac{37}{30} + \frac{7z}{15} + \frac{7z^2}{15} - \frac{2z^3}{15} + \frac{2z^4}{45} \quad (\text{C.41})$$

$$h_7(z) = \frac{37}{30} + \frac{79z}{105} - \frac{11z^2}{105} + \frac{14z^3}{45} - \frac{26z^4}{315} + \frac{4z^5}{315} \quad (\text{C.42})$$

$$h_8(z) = \frac{533}{420} + \frac{113z}{210} + \frac{113z^2}{210} - \frac{97z^3}{315} + \frac{113z^4}{630} - \frac{11z^5}{315} + \frac{z^6}{315} \quad (\text{C.43})$$

Along the centreline we have

$$v_x^{(2)}(x, 0) \approx -\frac{C^2}{32\pi^2\nu} \left[2\ln 2 \left(\frac{1}{x_0} - \frac{1}{x} \right) - \frac{(2x-x_0)(x-x_0)^2}{x^4} \times \right. \\ \left. \left(1 + \frac{7(x-x_0)^2}{6x^2} + \frac{37(x-x_0)^4}{30x^4} + \frac{533(x-x_0)^6}{420x^6} + \dots \right) \right] \quad (\text{C.44})$$

Eq. (C.21) can now be used to solve for $v_r^{(3)}$:

$$\frac{1}{r} \frac{\partial(rv_r^{(3)})}{\partial r} = -\frac{\partial v_x^{(2)}}{\partial x} \quad (\text{C.45})$$

Use Eq. (C.22) to eliminate the term in $\partial v_x^{(2)}/\partial x$,

$$\frac{1}{r} \frac{\partial(rv_r^{(3)})}{\partial r} = \frac{1}{\rho U} \frac{\partial p^{(2)}}{\partial x} - \frac{\nu}{Ur} \frac{\partial}{\partial r} \left(r \frac{\partial v_x^{(2)}}{\partial r} \right) \quad (\text{C.46})$$

so that

$$v_r^{(3)} = \frac{1}{\rho Ur} \int_0^r r \frac{\partial p^{(2)}}{\partial x} dr - \frac{\nu}{U} \frac{\partial v_x^{(2)}}{\partial r} \quad (\text{C.47})$$

Now

$$\frac{\partial p^{(2)}}{\partial x} = -\frac{\rho C^2 U}{32\pi^2 \nu} \frac{\partial}{\partial x} \left(\frac{f(z)}{x} \right) = \frac{\rho C^2 U (f(z) + z f'(z))}{32\pi^2 \nu x^2} \quad (\text{C.48})$$

Therefore

$$\begin{aligned} \frac{1}{\rho U r} \int_0^r r \frac{\partial p^{(2)}}{\partial x} dr &= \frac{C^2}{32\pi^2 \nu x^2 r} \int_0^r (f(z) + z f'(z)) r dr \\ &= \frac{C^2}{16\pi^2 x r U} \int_0^z (f(z) + z f'(z)) dz \\ &= \frac{C^2 z f(z)}{16\pi^2 x r U} \\ &= \frac{C^2 r}{64\pi^2 \nu x^2} f \left(\frac{r^2 U}{4\nu x} \right) \end{aligned} \quad (\text{C.49})$$

Moreover

$$\begin{aligned} \frac{\partial v_x^{(2)}}{\partial r} &= \frac{\partial v_x^{(2)}}{\partial z} \frac{\partial z}{\partial r} = \frac{2z}{r} \frac{\partial v_x^{(2)}}{\partial z} \\ &= -\frac{C^2 z}{16\pi^2 \nu r} \frac{\partial}{\partial z} \left[\left(f(z) - \frac{(1 - e^{-z})^2}{z} \right) \left(\frac{1}{x_0} - \frac{1}{x} \right) + \sum_{n=2}^{\infty} \frac{(x - x_0)^n}{x^{n+1}} h_n(z) e^{-2z} \right] \\ &= \frac{C^2 z}{16\pi^2 \nu r x} \left[\frac{2(1 - e^{-z})e^{-z}(x - x_0)}{z x_0} - \sum_{n=2}^{\infty} \frac{(x - x_0)^n}{x^n} q_n(z) e^{-2z} \right] \end{aligned} \quad (\text{C.50})$$

where

$$q_n(z) = h'_n(z) - 2h_n(z) \quad (\text{C.51})$$

The first few $q_n(z)$ are

$$q_1(z) = 0 \quad (\text{C.52})$$

$$q_2(z) = -2 \quad (\text{C.53})$$

$$q_3(z) = -\frac{4}{3} - \frac{4z}{3} \quad (\text{C.54})$$

$$q_4(z) = -2 - \frac{2z^2}{3} \quad (\text{C.55})$$

$$q_5(z) = -\frac{8}{5} - \frac{8z}{5} + \frac{8z^2}{15} - \frac{4z^3}{15} \quad (\text{C.56})$$

$$q_6(z) = -2 - \frac{4z^2}{3} + \frac{4z^3}{9} - \frac{4z^4}{45} \quad (\text{C.57})$$

$$q_7(z) = -\frac{12}{7} - \frac{12z}{7} + \frac{8z^2}{7} - \frac{20z^3}{21} + \frac{8z^4}{35} - \frac{8z^5}{315} \quad (\text{C.58})$$

$$q_8(z) = -2 - 2z^2 + \frac{4z^3}{3} - \frac{8z^4}{15} + \frac{4z^5}{45} - \frac{2z^6}{315} \quad (\text{C.59})$$

Therefore,

$$v_r^{(3)} = \frac{C^2 r}{64\pi^2 \nu x^2} \left[f(z) - \frac{2(1 - e^{-z})e^{-z}(x - x_0)}{zx_0} + \sum_{n=2}^{\infty} \frac{(x - x_0)^n}{x^n} q_n(z) e^{-2z} \right] \quad (\text{C.60})$$

Notice that $v_r^{(3)}$ is not identically zero on the initial plane. This is because the momentum flux due to the gradient of p in the axial direction must be balanced by a gradient in v_x : i.e. $\partial v_x^{(2)}/\partial x \neq 0$ in the initial plane. The continuity equation then requires that $v_r \neq 0$ in the initial plane.

The leading terms of each of the independent variables are now known.

$$v_x = U + v_x^{(2)} \epsilon^2 + o(\epsilon^3) \quad (\text{C.61})$$

$$v_r = v_r^{(3)} \epsilon^3 + o(\epsilon^4) \quad (\text{C.62})$$

$$v_\theta = \epsilon v_\theta^{(1)} + o(\epsilon^3) \quad (\text{C.63})$$

$$p = p^{(2)} \epsilon^2 + o(\epsilon^4) \quad (\text{C.64})$$

We proceed to the next level of expansion to get an idea of the error in these terms.

$$\frac{\partial v_x^{(3)}}{\partial x} + \frac{1}{r} \frac{\partial (r v_r^{(4)})}{\partial r} = 0 \quad (\text{C.65})$$

$$U \frac{\partial v_x^{(3)}}{\partial x} = \frac{\nu}{r} \frac{\partial}{\partial r} \left(r \frac{\partial v_x^{(3)}}{\partial r} \right) \quad (\text{C.66})$$

$$\frac{1}{\rho} \frac{\partial p^{(4)}}{\partial r} = \frac{2v_\theta^{(1)} v_\theta^{(3)}}{r} - U \frac{\partial v_r^{(3)}}{\partial x} + \nu \left(\frac{1}{r} \frac{\partial}{\partial r} \left(r \frac{\partial v_r^{(3)}}{\partial r} \right) - \frac{v_r^{(3)}}{r^2} \right) \quad (\text{C.67})$$

$$U \frac{\partial v_\theta^{(3)}}{\partial x} + \nu \left(\frac{v_\theta^{(3)}}{r^2} - \frac{1}{r} \frac{\partial}{\partial r} \left(r \frac{\partial v_\theta^{(3)}}{\partial r} \right) \right) = \nu \frac{\partial^2 v_\theta^{(1)}}{\partial x^2} - v_x^{(2)} \frac{\partial v_\theta^{(1)}}{\partial x} - v_r^{(3)} \frac{\partial v_\theta^{(1)}}{\partial r} \quad (\text{C.68})$$

Eq. (C.66) implies that $v_x^{(3)} = 0$, since it is zero on the upstream plane. Eq. (C.65) then implies that $v_r^{(4)} = 0$. Eq. (C.68) can be solved using the known expressions for the terms on the right hand side. Eq. (C.67) can then also be solved.

The first term on the right hand side of Eq. (C.68) is

$$\nu \frac{\partial^2 v_\theta^{(1)}}{\partial x^2} = -\frac{CUr}{32\pi x^3} \left(\frac{Ur^2}{\nu x} - 8 \right) e^{-\frac{Ur^2}{4\nu x}} = \frac{C}{4\pi} \sqrt{\frac{\nu U}{x^5}} (2 - z) \sqrt{z} e^{-z} \quad (\text{C.69})$$

The function $(2 - z)\sqrt{z} e^{-z}$ has a maximum value of 0.6902, so this term is bounded by

$$E_1 \sim \frac{0.69C}{4\pi} \sqrt{\frac{\nu U}{x^5}} \sim 0.055 C \sqrt{\frac{\nu U}{x^5}} \leq 0.055 C \sqrt{\frac{\nu U}{x_0^5}} = 0.025 \frac{\beta U^2 r_{ci}^2}{x_0^3} \quad (\text{C.70})$$

Since $|v_x^{(2)}|$ is largest on the centreline (see Figs. A.2, A.5 and A.8) and increases monotonically with x (see Figs. A.3, A.6 and A.9), we can estimate $v_x^{(2)}$ by evaluating Eq. (C.44) with $z = 0$ and $x = x_{mid} = 1.5x_0$. For $x < x_{mid}$,

$$v_x^{(2)} < -1.1 \times 10^{-3} \frac{C^2}{\nu x_0} = -5.5 \times 10^{-3} \beta^2 U \quad (\text{C.71})$$

Since

$$\frac{\partial v_\theta^{(1)}}{\partial x} = \frac{CUr}{8\pi\nu x^2} e^{-\frac{Ur^2}{4\nu x}} = \frac{C}{4\pi} \sqrt{\frac{Uz}{\nu x^3}} e^{-z} \quad (\text{C.72})$$

and since $\sqrt{z} e^{-z}$ has a maximum of 0.4289,

$$\frac{\partial v_\theta^{(1)}}{\partial x} \leq 0.4289 \frac{C}{4\pi} \sqrt{\frac{U}{\nu x^3}} \leq 0.034 C \sqrt{\frac{U}{\nu x_0^3}} = 0.076 \frac{\beta U}{x_0} \quad (\text{C.73})$$

Therefore the second term on the right hand side of Eq. (C.68) is of order

$$E_2 \sim -v_x^{(2)} \frac{\partial v_\theta^{(1)}}{\partial x} \sim -4.2 \times 10^{-4} \frac{\beta^3 U^2}{x_0} \quad (\text{C.74})$$

From Eqs. (C.10) and (C.60), the third term on the right hand side of Eq. (C.68) is

$$\begin{aligned} E_3 &= -v_r^{(3)} \frac{\partial v_\theta^{(1)}}{\partial r} \\ &= \frac{C^3}{256\pi^3} \sqrt{\frac{U}{\nu^3 x^5}} \left[f(z) - \frac{2(1 - e^{-z})e^{-z}(x - x_0)}{zx_0} + \sum_{n=2}^{\infty} \frac{(x - x_0)^n}{x^n} q_n(z) e^{-2z} \right] \times \\ &\quad \sqrt{z} \left(2e^{-z} - \frac{(1 - e^{-z})}{z} \right) \end{aligned} \quad (\text{C.75})$$

For $x < x_{mid}$, the complicated term in z has a maximum of about 0.4 occurring on the initial plane. Therefore for $x < x_{mid}$ we have

$$E_3 \leq 0.4 \frac{C^3}{256\pi^3} \sqrt{\frac{U}{\nu^3 x^5}} \leq 5 \times 10^{-5} C^3 \sqrt{\frac{U}{\nu^3 x_0^5}} \approx 6 \times 10^{-4} \frac{\beta^3 U^2}{x_0} \quad (\text{C.76})$$

Since for the values of β used in our calculations, $\beta \gg r_{ci}/x_0$, E_1 is significantly smaller than E_2 and E_3 , while E_2 and E_3 are of similar size. Therefore we can approximate the magnitude of the right hand side of Eq. (C.68) by E_3 . Then we can estimate that

$$\frac{\partial v_\theta^{(3)}}{\partial x} \sim \frac{E_3}{U} = 6 \times 10^{-4} \frac{\beta^3 U}{x_0} \quad (\text{C.77})$$

and therefore at $x = x_{mid}$

$$v_{\theta}^{(3)} \sim (x_{mid} - x_0) \frac{\partial v_{\theta}^{(3)}}{\partial x} = 9 \times 10^{-4} \beta^3 U \quad (\text{C.78})$$

The maximum value of $v_{\theta}^{(1)}$ at the mid-plane is $0.093\beta U$. Therefore the relative error in the approximation of v_{θ} by $\epsilon v_{\theta}^{(1)}$ is

$$E \sim \frac{9 \times 10^{-4} \beta^3 U}{0.093 \beta U} \approx 0.01 \beta^2 \quad (\text{C.79})$$

In practice this is a conservative estimate, both because we have used maximum values when estimating the size of the error terms, and because we have neglected the diffusive term in the estimate of [Eq. \(C.77\)](#).

When $\beta = 0.0446$, $E \approx 2 \times 10^{-5}$ and when $\beta = 0.446$, $E \approx 2 \times 10^{-3}$. Therefore for these values of β the approximate solution is very good and we should expect the numerical solutions to converge to it. When $\beta = 4.46$, $E \approx 0.2$ so that we should expect differences of the order of 20% between the numerical and approximate solution. This is roughly consistent with the results shown in [Fig. A.7](#).

Of the terms on the right hand side of [Eq. \(C.67\)](#), the first is proportional to β^4 while the others are proportional to $\beta^2 r_{ci}^2 / x_0^2$. Therefore the first term is dominant for the values of β that we have used. Comparing this term to $(v_{\theta}^{(1)})^2 / r$, which is the equivalent term for the radial gradient of $p^{(2)}$, suggests that the relative error in the approximation of p is approximately twice the relative error in v_{θ} . Again, this is roughly consistent with the results shown in [Fig. A.7](#).

List of symbols

α	Constant of proportionality relating ν_t and C for a fully-developed turbulent vortex: $\nu_t \approx \alpha C$.
β	Non-dimensionalized circulation: $C/U r_{ci}$.
ν	Kinematic viscosity.
ν_t	Turbulent kinematic eddy viscosity.
C	The circulation of the vortex.
C_p	The pressure coefficient: $C_p = p/\frac{1}{2}\rho U^2$.
J	Advance coefficient.
N_θ	The number of nodes around the circumference of the hexahedral grid.
N_c	The number of nodes across the vortex core.
N_r	The number of nodes radially in the hexahedral grid.
N_x	The number of nodes in the x direction in the hexahedral and prismatic grids.
p	Pressure.
(r, θ, x)	Cylindrical coordinates.
r_c	The radius of the vortex core.
r_{ci}	The radius of the vortex core in the upstream plane.
R	The outer radius of the grid.
s_0	The distance between radial nodes at $r = 0$ in the hexahedral grid.
s_R	The distance between radial nodes at $r = R$ in the hexahedral grid.
U	The magnitude of the free-stream velocity.
(v_x, v_r, v_θ)	Components of the velocity in a cylindrical coordinate system.
V	Speed of advance of a propeller.
V_r	Radial component of velocity past a propeller. The radial direction is relative to the propeller axis.

x_0	The x coordinate of the upstream end of the grid.
x_{mid}	The x coordinate halfway down the grid.
x_1	The x coordinate of the downstream end of the grid.

Distribution list

DRDC Atlantic TM 2009-052

Internal distribution

- 1 Author
- 1 G. Watt
- 3 Library

Total internal copies: 5

External distribution

Department of National Defence

- 1 DRDKIM
- 2 DMSS 2

Others

- 1 Prof. Andrew Gerber
Dept. of Mechanical Engineering
University of New Brunswick
P.O. Box 4400
Fredericton, New Brunswick
E3B 5A3
- 1 Prof. Gordon Holloway
Dept. of Mechanical Engineering
University of New Brunswick
P.O. Box 4400
Fredericton, New Brunswick
E3B 5A3
- 1 Library and Archives Canada
395 Wellington Street
Ottawa, Ontario
K1A 0N4
Attn: Military Archivist, Government Records Branch

- 1 Director-General
Institute for Marine Dynamics
National Research Council of Canada
P.O. Box 12093, Station A
St. John's, Newfoundland
A1B 3T5
- 1 Director-General
Institute for Aerospace Research
National Research Council of Canada
Building M-13A
Ottawa, Ontario
K1A 0R6
- 1 Transport Development Centre
Transport Canada
6th Floor
800 Rene Levesque Blvd, West
Montreal, Quebec
H3B 1X9
Attn: Marine R&D Coordinator
- 1 Canadian Coast Guard
Ship Safety Branch
Canada Building, 11th Floor
344 Slater Street
Ottawa, Ontario
K1A 0N7
Att: Chief, Design and Construction

MOUs

- 6 Canadian Project Officer ABCA-02-01 (C/SCI, DRDC Atlantic – 3 paper copies, 3 PDF files on CDROM)

Total external copies: 16

Total copies: 21

DOCUMENT CONTROL DATA		
(Security classification of title, body of abstract and indexing annotation must be entered when document is classified)		
1. ORIGINATOR (The name and address of the organization preparing the document. Organizations for whom the document was prepared, e.g. Centre sponsoring a contractor's report, or tasking agency, are entered in section 8.) Defence R&D Canada – Atlantic PO Box 1012, Dartmouth NS B2Y 3Z7, Canada	2. SECURITY CLASSIFICATION (Overall security classification of the document including special warning terms if applicable.) UNCLASSIFIED	
3. TITLE (The complete document title as indicated on the title page. Its classification should be indicated by the appropriate abbreviation (S, C or U) in parentheses after the title.) RANS calculations of the evolution of vortices on unstructured grids		
4. AUTHORS (Last name, followed by initials – ranks, titles, etc. not to be used.) Hally, D.		
5. DATE OF PUBLICATION (Month and year of publication of document.) November 2009	6a. NO. OF PAGES (Total containing information. Include Annexes, Appendices, etc.) 68	6b. NO. OF REFS (Total cited in document.) 8
7. DESCRIPTIVE NOTES (The category of the document, e.g. technical report, technical note or memorandum. If appropriate, enter the type of report, e.g. interim, progress, summary, annual or final. Give the inclusive dates when a specific reporting period is covered.) Technical Memorandum		
8. SPONSORING ACTIVITY (The name of the department project office or laboratory sponsoring the research and development – include address.) Defence R&D Canada – Atlantic PO Box 1012, Dartmouth NS B2Y 3Z7, Canada		
9a. PROJECT OR GRANT NO. (If appropriate, the applicable research and development project or grant number under which the document was written. Please specify whether project or grant.) Project 11cd23	9b. CONTRACT NO. (If appropriate, the applicable number under which the document was written.)	
10a. ORIGINATOR'S DOCUMENT NUMBER (The official document number by which the document is identified by the originating activity. This number must be unique to this document.) DRDC Atlantic TM 2009-052	10b. OTHER DOCUMENT NO(s). (Any other numbers which may be assigned this document either by the originator or by the sponsor.)	
11. DOCUMENT AVAILABILITY (Any limitations on further dissemination of the document, other than those imposed by security classification.) (X) Unlimited distribution () Defence departments and defence contractors; further distribution only as approved () Defence departments and Canadian defence contractors; further distribution only as approved () Government departments and agencies; further distribution only as approved () Defence departments; further distribution only as approved () Other (please specify):		
12. DOCUMENT ANNOUNCEMENT (Any limitation to the bibliographic announcement of this document. This will normally correspond to the Document Availability (11). However, where further distribution (beyond the audience specified in (11)) is possible, a wider announcement audience may be selected.)		

13. ABSTRACT (A brief and factual summary of the document. It may also appear elsewhere in the body of the document itself. It is highly desirable that the abstract of classified documents be unclassified. Each paragraph of the abstract shall begin with an indication of the security classification of the information in the paragraph (unless the document itself is unclassified) represented as (S), (C), or (U). It is not necessary to include here abstracts in both official languages unless the text is bilingual.)

The evolution of laminar vortices was calculated using the Reynolds-averaged Navier-Stokes solver ANSYS CFX. Vortices of different strengths were modelled on unstructured grids using different element types and different node densities, then compared to an approximate solution of the Navier-Stokes equation. Grids using hexahedral or prismatic elements aligned with the vortex yielded significantly more accurate solutions than tetrahedral grids, especially when the circulating velocity was much smaller than the convection velocity. Over-diffusion of the circumferential velocity is the major source of error in these solutions.

ANSYS CFX was also used to determine the effect of grid density on a turbulent vortex, though in this case there is no analytic solution to compare with. As with the laminar vortex, grids using hexahedral or prismatic elements aligned with the vortex converge much more rapidly with cell size than tetrahedral grids, suggesting that they are more accurate. In these solutions the over-diffusion of turbulent viscosity by artificial viscosity is an important source of error.

The solutions are used to make recommendations for the density of unstructured grids required for accurate predictions of the pressure in the core as the vortex evolves over hundreds of core diameters.

14. KEYWORDS, DESCRIPTORS or IDENTIFIERS (Technically meaningful terms or short phrases that characterize a document and could be helpful in cataloguing the document. They should be selected so that no security classification is required. Identifiers, such as equipment model designation, trade name, military project code name, geographic location may also be included. If possible keywords should be selected from a published thesaurus. e.g. Thesaurus of Engineering and Scientific Terms (TEST) and that thesaurus identified. If it is not possible to select indexing terms which are Unclassified, the classification of each should be indicated as with the title.)

Computational fluid dynamics

Fluid flow

Vortex flows

ANSYS CFX

CFX-TASCflow

TRANSOM

This page intentionally left blank.

Defence R&D Canada

Canada's leader in defence
and National Security
Science and Technology

R & D pour la défense Canada

Chef de file au Canada en matière
de science et de technologie pour
la défense et la sécurité nationale



www.drdc-rddc.gc.ca